IOP Publishing New J. Phys. 18 (2016) 093006 doi:10.1088/1367-2630/18/9/093006

New Journal of Physics
The open access journal at the forefront of physics

Deutsche Physikalische Gesellschaft DPG
IOP Institute of Physics
Published in partnership with: Deutsche Physikalische Gesellschaft and the Institute of Physics

PAPER

Antipolar ordering of topological defects in active liquid crystals

Anand U Oza[1] **and Jörn Dunkel**[2]

[1] Courant Institute of Mathematical Sciences, 251 Mercer Street, New York, NY 10012, USA
[2] Department of Mathematics, Massachussetts Institute of Technology, 77 Massachusetts Avenue, Cambridge, MA 02139-4307, USA

E-mail: dunkel@mit.edu

CrossMark

OPEN ACCESS

RECEIVED
19 April 2016

REVISED
7 August 2016

ACCEPTED FOR PUBLICATION
10 August 2016

PUBLISHED
8 September 2016

Keywords: active liquid crystals, Landau-de Gennes free-energy, Stokes flow

Supplementary material for this article is available online

Abstract

ATP-driven microtubule-kinesin bundles can self-assemble into two-dimensional active liquid crystals (ALCs) that exhibit a rich creation and annihilation dynamics of topological defects, reminiscent of particle-pair production processes in quantum systems. This recent discovery has sparked considerable interest but a quantitative theoretical description is still lacking. We present and validate a minimal continuum theory for this new class of active matter systems by generalizing the classical Landau–de Gennes free-energy to account for the experimentally observed spontaneous buckling of motor-driven extensile microtubule bundles. The resulting model agrees with recently published data and predicts a regime of antipolar order. Our analysis implies that ALCs are governed by the same generic ordering principles that determine the non-equilibrium dynamics of dense bacterial suspensions and elastic bilayer materials. Moreover, the theory manifests an energetic analogy with strongly interacting quantum gases. Generally, our results suggest that complex nonequilibrium pattern-formation phenomena might be predictable from a few fundamental symmetry-breaking and scale-selection principles.

Active materials [1] assembled from intracellular components, such as DNA [2], microtubules and motor proteins [3–5] promise innovative biotechnological applications, from microscale transport and medical devices [2] to artificial tissues [1] and programmable soft materials [6–8]. Beyond their practical value, these systems challenge theorists to generalize equilibrium statistical mechanics to far-from-equilibrium regimes [9–26]. Recent experimental advances in the self-assembly and manipulation of colloids with DNA-mediated interactions [27–29] have stimulated theoretical analysis that may eventually help clarify the physical principles underlying self-replication [30–32] and evolution in viruses [33–35] and other basic biological systems. Yet, despite some partial progress [10, 18, 19, 36–39], our conceptual understanding of active materials, and living matter in general, remains far from complete. We do not know whether, or under which conditions, ‘universality’ ideas [40] that have proved powerful in the description of equilibrium systems can be generalized to describe collective dynamics of active matter not just qualitatively but also quantitatively. This deficit may be ascribed to the fact that mathematical models have been successfully tested against experiments in only a few instances [3, 4, 15, 41–43].

Recently discovered 2D active liquid crystal (ALC) analogs [5, 44–47] comprise an important class of non-equilibrium systems that allows further tests of general theoretical concepts [40] and specific models. ALCs are assemblies of rod-like particles that exhibit non-thermal collective excitations due to steady external [44, 45] or internal [5, 47] energy input. At high concentrations, ALCs form an active nematic phase characterized by dynamic creation and annihilation of topological defects [5, 44, 47], reminiscent of spontaneous particle-pair production in quantum systems. This phenomenon was demonstrated recently [5, 47, 48] for ATP-driven microtubule-kinesin bundles trapped in flat and curved interfaces. Moreover, these experiments [48] revealed an unexpected nematic ordering of topological defects which is unaccounted for in current theoretical models.

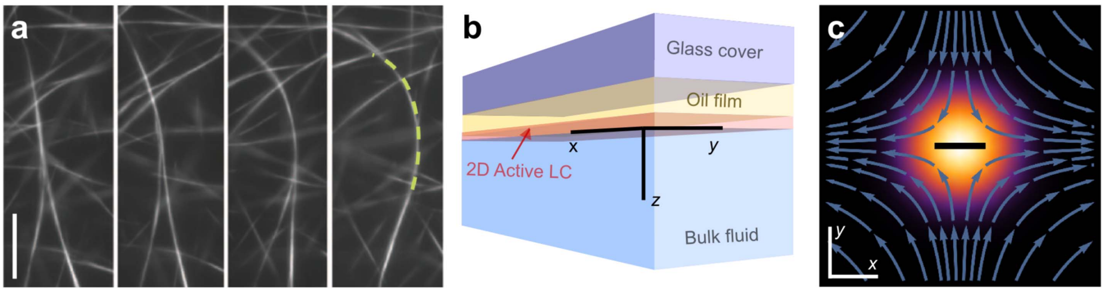

Figure 1. (a) Image sequence showing spontaneous buckling of a microtubule bundle (dashed) caused by extensile ATP-driven motor activity, adapted with permission from figure 1(c) in [5]. Time interval 11.5 s, scale bar 15 μm. For a passive or contractile bundle, one would expect straightening instead of bending, approximately corresponding to a time-reversal of the depicted sequence.
(b) Schematic of the experimental setup reported in [5, 48], not drawn to scale. A thin oil film (thickness $\sim 3\ \mu$m) separates a 2D ALC layer ($\sim$0.2–1.0 μm) at the oil-water interface from a solid glass cover. Liquid can be exchanged between the ALC layer and bulk fluid, resulting in compressible 2D interfacial flow that is strongly damped by the nearby no-slip glass boundary and the viscous oil layer.
(c) Extensile 2D dipole flow in the interface as predicted by the overdamped closure condition (4) for $D > 0$ and $Q = (\lambda,\ 0;\ 0,\ -\lambda)$ with $\lambda = \exp(-\boldsymbol{r}^2)$. The central horizontal bar indicates the unit director axis, and background colors the nematic order parameter $S \sim \lambda$.

Understanding the emergence of such topological super-structures is crucial for the development and control of new materials, as recently demonstrated for colloidal liquid crystals [49–51].

We here develop and test a closed continuum theory for dense ALCs by generalizing the higher-order scalar and vector theories of soft elastic materials [52] and bacterial fluids [15, 41] to matrix-valued fields. Specifically, we propose a modification of the commonly adopted Landau–de Gennes (LdG) free energy to account for the inherently different microscopic buckling behaviors of passive and active LCs [5]. While bending is energetically unfavorable in passive LCs and hence penalized by the LdG energy functional, kinesin-driven ALCs buckle spontaneously even at low concentrations due to the extensile motor action (figure 1(a)). This experimental observation [5] implies that the classical LdG framework is, by construction, ill-suited to describe experiments in which microtubule bundles are sheared relative to each other by motor proteins [5, 47, 48]. The inclusion of active bending effects in the LdG functional yields a tensor version of the Swift–Hohenberg theory [53] of pattern formation. The resulting minimal model has only two dimensionless parameters, thus allowing a detailed comparison with recent experimental data [5, 48].

In addition to the traditional Q-tensor formulation, we present an equivalent complex scalar field representation [14, 54] that manifests an analogy with a generalized Gross–Pitaevskii theory [55, 56] of strongly coupled many-body quantum systems [57–60]. In the case of normal dispersion, the celebrated LC-superconductor correspondence [54, 61] has helped elucidate profound parallels between the smectic phase in passive LCs and the Abrikosov vortex lattices in type-II superconductors [62, 63]. The results below indicate that a similar analogy may exist between ALCs and Bose–Einstein/Fermi condensates with double-well dispersion [58–60], suggesting that ALCs could offer insights into the dynamics of these quantum systems and vice versa.

Results

Experimental conditions

Recent experiments [5, 48] show that ATP-driven microtubule-kinesin bundles can self-assemble into a dense quasi-2D ALC layer at a surfactant-supported oil-water interface parallel to a planar solid boundary (figure 1(b)). This 'wet' ALC was found to exhibit local nematic alignment of bundles, persistent annihilation and creation dynamics of topological defects [5], and remarkable nematic order of the defect orientations in thin layers [48]. Although a large number of unknown parameters has prevented detailed quantitative comparisons between theory and experiment, several recently proposed multi-order-parameter models of 2D ALC systems [14, 20, 64, 65] were able to reproduce qualitatively selected aspects of these observations, such as defect-pair creation and separation [65]. Despite providing some important insights, traditional models often do not account for three relevant details of the experiments [5, 48]. First, those models typically assume divergence-free 2D fluid flow within the ALC layer, which is a valid approximation for isolated free-standing film experiments [66] but neglects fluid exchange between the 2D interface and bulk in the ALC experiments (figure 1(b)). Indeed, the surfactant-stabilized interface causes the microtubule-kinesin bundles to assemble into a quasi-2D layer, but places no such constraint on the fluid. As is known for classical turbulence [67, 68], small-scale energy input can trigger turbulent upward cascades in incompressible 2D flow. Thus, topological defect dynamics in the current standard models may be dominated by artificially enhanced

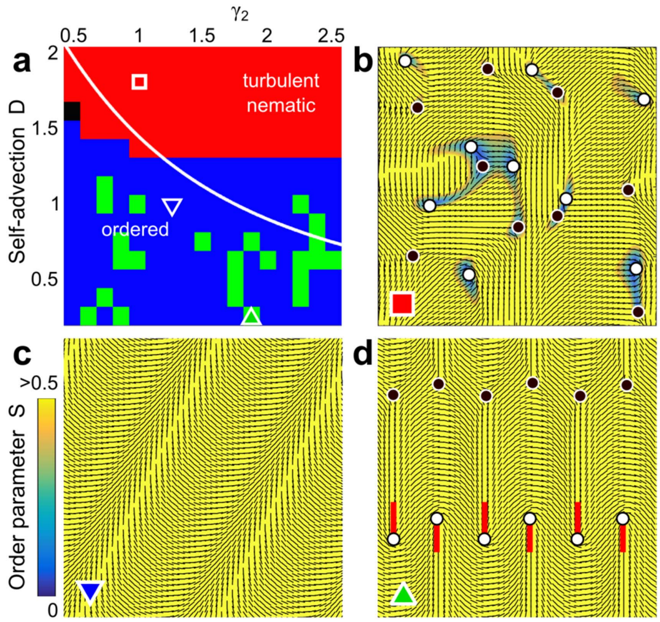

Figure 2. Phase diagram obtained from simulations of equation (8) for one particular set of random initial conditions showing the emergence of turbulent nematic states for supercritical active self-advection. (a) We observe convergence to defect-free stripes (blue, panel (c), Movie S3), long-lived static and oscillatory defect lattice solutions (green, panel (d), Movie S4), oscillatory defect creation and annihilation events (black, Movies S6 and S7), and chaotic dynamics (red, panel (b), Movie S1). The white line indicates the analytical estimate $D_c = 2(-\gamma_2 + \sqrt{\gamma_2^2 + 2})$ for the transitions between ordered and chaotic states. (b)–(d) Examples of the states identified in panel (a) with $-\frac{1}{2}$-defects (black) and $+\frac{1}{2}$–defects (white). Panel (d) highlights the antipolar ordering of $+\frac{1}{2}$-defect orientations (red bars); see also figure 3 and Movie S5 for a realization of this state in a $\sim 10\times$ larger simulation domain.

hydrodynamic mixing due to a simplifying 2D incompressibility assumption that is unlikely to hold under realistic experimental conditions [5, 48]. Second, a relevant yet previously ignored effect is damping from the nearby boundaries, which may promote topological defect ordering. Third, as already mentioned above, the commonly adopted standard LdG free-energy functional does *not* account for motor-driven spontaneous buckling [5] of microtubule bundles (figure 1(a)), which is one of the key differences between passive and active LCs (Z. Dogic, private communication). To overcome such limitations and achieve a quantitative description of the experiments [5, 48], we next construct a closed continuum theory for ALCs described by a nematic tensor field $Q(t, \boldsymbol{r})$. The theory accounts for the different buckling behaviors of passive and active LCs and builds on a self-consistent hydrodynamic closure condition.

Theory

Traditional multi-field models [64, 65] aim to describe the 2D nematic phase of a dense ALC suspension by coupling the filament concentration $c(t, \boldsymbol{r})$ and the nematic order tensor $Q(t, \boldsymbol{r})$ to an incompressible 2D flow field $\boldsymbol{v}(t, \boldsymbol{r})$ that satisfies $\nabla \cdot \boldsymbol{v} = 0$ in the interface plane $\boldsymbol{r} = (x, y)$. The nematic order parameter $S(t, \boldsymbol{r})$ is proportional to the larger eigenvalue of Q, and the filaments are oriented along the corresponding eigenvector, or director $\boldsymbol{n}(t, \boldsymbol{r})$. To construct an alternative closed-form theory for the symmetric traceless 2×2-tensor field Q, we start from the generic transport law

$$\partial_t Q + \nabla \cdot (\boldsymbol{v} Q) - \kappa[Q, \omega] = -\frac{\delta \mathcal{F}}{\delta Q}, \qquad (1)$$

where $\omega = [\nabla \boldsymbol{v} - (\nabla \boldsymbol{v})^{\top}]/2$ is the vorticity tensor, $[A, B] = AB - BA$ the commutator of two matrices and $\mathcal{F}[Q] = \int d^2 r\ F$ an effective free energy. Focussing on dense suspensions as realized in the experiments [5, 48], we neglect fluctuations in the microtubule concentration, $\nabla c \equiv 0$. A derivation of the advection term $\nabla \cdot (\boldsymbol{v} Q)$ from the probability conservation laws underlying generic advection-diffusion models is outlined in the supplementary information. It is important, however, that $\nabla \cdot (\boldsymbol{v} Q) \neq \boldsymbol{v} \cdot \nabla Q$ when $\nabla \cdot \boldsymbol{v} \neq 0$, which is typically the case when fluid can enter and leave the interface. Combining LdG theory [69] with Swift–Hohenberg theory [53], we consider the effective non-equilibrium free-energy density (supplementary information)

$$F = \mathrm{Tr}\left\{-\frac{a}{2}Q^2 + \frac{b}{4}Q^4 - \frac{\gamma_2}{2}(\nabla Q)^2 + \frac{\gamma_4}{4}(\nabla\nabla Q)^2\right\} \tag{2}$$

with $a,\ b > 0$ for the nematic phase. Assuming γ_2 can have either sign, ultraviolet stability requires $\gamma_4 > 0$. For $\gamma_2 < 0$, F penalizes bending and buckling, as is appropriate for passive LCs and possibly 'dry' shaken nematics [44, 45], forcing the system dynamics towards a homogeneous nematic ground-state manifold. By contrast, motor-induced spontaneous buckling [5] (figure 1(a)) of kinesin-driven ALCs demands $\gamma_2 > 0$, and consequently patterns of characteristic wavelength $\Lambda \sim \sqrt{\gamma_4/\gamma_2}$ become energetically favorable, as shown below.

The requirement $\gamma_2 > 0$ for ALCs has an intrinsically microscopic origin, as the ALC assembly consists of microtubules that grow against each other and spontaneously buckle due to the motor-induced extensile shear dynamics of adjacent bundles (figure 1(a)). To explain this important point in more detail, let us recall that passive LCs are modeled using $\gamma_2 < 0$, as the corresponding term in the free energy penalizes variations in Q and thus inhibits spatial inhomogeneities at damping rate $\gamma_2 k^2 < 0$ in Fourier space. Microscopically, the alignment dynamics of two rod-like passive LC molecules roughly corresponds to a time-reversal of the ALC pair-interaction image sequence in figure 1(a), implying that a corresponding ALC system would develop buckling instabilities at growth rate $\gamma_2 k^2 > 0$. Additional empirical support for this theoretical picture comes from a comparison of the experimentally observed length scales in ALC systems: the microtubule-kinesin bundles realized in the ALC experiments [5, 48] are approximately 10–30 μm in length (figure 1(b) in [5]), which is on the same scale as both the spontaneous buckling wavelength (figures 1(c) and (d) in [5], and figure 1(a)) and the typical separation distance between defects (bottom panels of figure 3(d) in [5], reproduced in figure 4(a) below). That is, there exists no substantial scale separation between the buckling microscopic constituents and emergent ALC dynamics.

Similar buckling phenomena are generically observed in many systems that are subjected to external or internal stresses, for example in elastic films and sheets [52, 70] and in geometrically confined cellular networks [71, 72]. The ALCs experience an effective compressive stress due to the extensile 'growth' of the filament pairs in a confined geometry, which arises from their motor-induced shear dynamics. Application of such a compressive stress leads to buckling of the network's constituents [71, 72]. It has been shown that out-of-plane buckling of an elastic sheet due to an effective compressive stress may be quantitatively modeled by a Swift–Hohenberg-type equation with $\gamma_2 > 0$ in the corresponding free energy [52]. We expect the same to be true for the in-plane buckling of microtubules confined to a planar interface, and thus analyze here an effective theory that incorporates this spontaneous motor-induced buckling phenomenologically through $\gamma_2 > 0$.

Hydrodynamic closure

To obtain a closed Q-model, we relate the 2D flow field $\boldsymbol{v}$ to Q through the linearly damped Stokes equation [73, 74]

$$-\eta\nabla^2\boldsymbol{v} + \nu\boldsymbol{v} = -\zeta\nabla\cdot Q, \tag{3}$$

where η is the viscosity and the rhs represents active stresses [10, 64] with $\zeta > 0$ for extensile ALCs (figure 1(c)). A pressure term does not appear in equation (3) because the interfacial flow is not assumed to be incompressible and concentration fluctuations are neglected. The ν-term in the force balance (3) has been used to model interfacial damping in other contexts, such as surfactant membranes on a solid substrate [73], and accounts for friction from the nearby no-slip boundary in the Hele–Shaw [74] approximation (figure 1(b)). In the overdamped regime $\nu\Lambda^2/\eta \gg 1$, we deduce from equation (3) the closure condition

$$\boldsymbol{v} = -D\nabla\cdot Q, \qquad D = \zeta/\nu. \tag{4}$$

Equation (4) is conceptually similar to closure conditions proposed previously for active polar films [75]. Importantly, equation (4) predicts divergent interfacial flow, $\nabla\cdot\boldsymbol{v} \neq 0$, and hence fluid transport perpendicular to the interface wherever $\nabla\nabla : Q \neq 0$. Inserting (4) into (1) yields a closed Q-theory in which periodic director patterns corresponding to local minima of the free energy $\mathcal{F}$ can become mixed by self-generated interfacial flow.

Complex representation and ALC-quantum analogy

The traditional characterization of 2D nematic order in terms of the symmetric traceless 2×2 matrix field $Q = (\lambda,\ \mu;\ \mu,\ -\lambda)$ is redundant, for only two real scalar fields $\lambda(t,\ \boldsymbol{r})$ and $\mu(t,\ \boldsymbol{r})$ are needed to specify the nematic state at each position $\boldsymbol{r} = (x,\ y)$. To obtain an irreducible representation [14, 54] we define the complex position coordinate $z = x + \mathrm{i}y$, velocity field $v(t,\ z) = u + \mathrm{i}w$ and complex order parameter $\psi(t,\ z) = \lambda + \mathrm{i}\mu$, such that $S = 2|\psi|$. In terms of the Wirtinger gradient operator $\partial = \frac{1}{2}(\partial_x - \mathrm{i}\partial_y)$, the 2D Laplacian takes the form $\nabla^2 = 4\bar{\partial}\partial$ and the closure condition (4) reduces to $v = -2D\partial\psi$. Denoting the real and imaginary parts of an operator $\mathcal{O}$ by $\mathfrak{R}\{\mathcal{O}\}$ and $\mathfrak{I}\{\mathcal{O}\}$, equations (1) and (2) may be equivalently expressed as

$$\partial_t\psi + \mathcal{A}_\psi\psi = -\frac{\delta\mathcal{G}}{\delta\bar{\psi}}, \tag{5}$$

where the self-advection operator is given by

$$\mathcal{A}_\psi = -4D\,\Re\{(\partial^2\psi) + (\partial\psi)\partial\} + 4\kappa D\,\mathrm{i}\,\Im\{\partial^2\psi\} \tag{6}$$

and the free energy $\mathcal{G}[\psi, \bar{\psi}] = \int \mathrm{d}z\ G$ has the density

$$G = -a|\psi|^2 + \frac{b}{2}|\psi|^4 + \gamma_2\bar{\psi}(4\bar{\partial}\partial)\psi + \gamma_4\bar{\psi}(4\bar{\partial}\partial)^2\psi. \tag{7}$$

For $\gamma_2 < 0$ and $\gamma_4 \to 0$, equation (7) reduces to the energy density of the Gross–Pitaevskii mean-field model [55, 56] for weakly interacting boson gases. Historically, this limit case has been crucial [54, 61] for elucidating the analogy between the smectic phase of passive LCs and the Abrikosov flux lattice in type-II superconductors [62, 63]. For $\gamma_2, \gamma_4 > 0$, equation (7) effectively describes double-well dispersion [57], as recently realized for quasi-momenta in spin–orbit-coupled Bose–Einstein condensates [58, 60] and Fermi gases [59]. This fact establishes an interesting connection between dense ALCs and strongly coupled quantum systems: when self-advection is negligible ($D \to 0$), the fixed point configurations of equation (5) coincide with the 'eigenstates' of generalized Gross–Pitaevskii models that incorporate wavelength selection.

Stability analysis

The qualitative model dynamics is not significantly altered for moderate values of κ (Movies S1 and S2), so we neglect the commutator term by setting $\kappa = 0$ from now on (see supplementary information for $\kappa > 0$). To understand the properties of equations (5) and (6) when self-advection is relevant, we perform a fixed point analysis of the rescaled dimensionless equation (supplementary information)

$$\partial_t\psi - 4D\,\Re\{(\partial^2\psi) + (\partial\psi)\partial\}\,\psi = \left(\frac{1}{4} - |\psi|^2\right)\psi - \gamma_2(4\bar{\partial}\partial)\psi - (4\bar{\partial}\partial)^2\psi, \tag{8}$$

by focussing on the uniform state $\psi_* = \frac{1}{2}\mathrm{e}^{\mathrm{i}2\theta}$, which corresponds to a nematic order parameter value $S = 1$and homogeneous director angle θ relative to the x-axis. Considering wave-like perturbations $\psi = \psi_* + \hat{\epsilon}(t)\mathrm{e}^{\mathrm{i}\boldsymbol{k}\cdot\boldsymbol{r}}$ with $|\hat{\epsilon}| \ll 1$ and extensile ALCs with $D > 0$, one finds that ψ_* is unstable when $\gamma_2 > 0$ (supplementary information). For subcritical self-advection, $D < D_c = 2(-\gamma_2 + \sqrt{\gamma_2^2 + 2})$, the dominant instability is driven by modes with wavenumber $|\boldsymbol{k}| = \sqrt{\gamma_2/(2\gamma_4)}$, suggesting the formation of stripe patterns with typical wavelength $\Lambda \approx \sqrt{8\pi^2\gamma_4/\gamma_2}$. By contrast, for supercritical advection, $D > D_c$, the most unstable mode propagates perpendicular to the director, $(k_*, \phi_*) = (\sqrt{(2\gamma_2 + D)/(4\gamma_4)}, \theta + (\pi/2))$, suggesting the possibility of transverse mixing.

Phase diagram

To investigate the nonlinear dynamics of equation (8), we implemented a Fourier pseudospectral algorithm with modified Runge–Kutta time-stepping [76] (Methods) and so evolved the real and imaginary parts of $\psi(t, z)$ in time for periodic boundary conditions in space. A numerically obtained (γ_2, D)-phase diagram for random initial conditions confirms the existence of a turbulent nematic phase if active self-advection is sufficiently strong (figures 2(a) and (b); Movie S1). Ordered configurations prevail at low activity (figures 2(a), (c) and (d); Movies S3, S4 and S6). Although the ground-states of the free energy (2) are in general not homogeneous, the critical curve separating the two regimes is in fair agreement with the estimate $D_c = 2(-\gamma_2 + \sqrt{\gamma_2^2 + 2})$ from linear stability of the homogenous state (white line in figure 2(a)). For subcritical values of the advection parameter D, we observe either defect-free ground-states or long-lived lattice-like states exhibiting ordered defect configurations (figures 2(c) and (d)). Regarding the subsequent comparison between theory and experiment, it is important to note that the lattices are also found in simulations with a large domain (figure 3; Movie S5). These spatially periodic states generally exhibit antipolar long-range ordering of $+\frac{1}{2}$-defects (figures 2(d); 3(a)) accompanied by vortex flow lattices (figure 3(c)). Numerical free-energy calculations show that defect-free states (figure 2(c)) typically have slightly lower energies than the lattice states (figure 2(d)), leaving open the possibility of a very slow decay of the latter. However, regardless of whether such lattice states are extremely long-lived metastable or truly stable states, these simulation results confirm that anti polar ordering of $+\frac{1}{2}$-defect pairs can persist over experimentally relevant time-scales.

Theory versus experiment

To test our theory systematically against existing experimental data [5, 48], we analyze defect-pair dynamics, global defect ordering and defect statistics in the turbulent nematic phase.

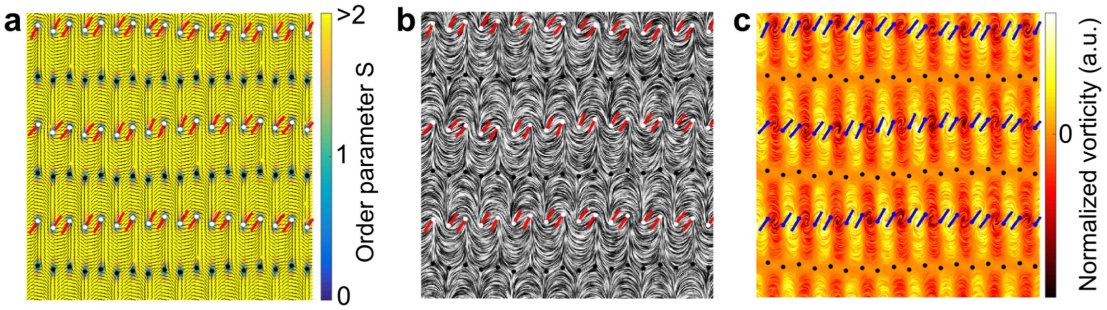

Figure 3. Vortex lattice states with antipolar long-range ordering of nematic defects, see also Movie S5. (a) Long-lived nematic order parameter field with periodically aligned $-\frac{1}{2}$-defects (black) and $+\frac{1}{2}$-defects (red). (b) Line integral convolution (LIC) plot of the corresponding director field as a proxy for microtubule-bundle patterns. (c) LIC plot of the corresponding fluid velocity field, color-coded by normalized vorticity, demonstrates the formation of a vortex flow lattice. Dimensionless simulation parameters are $D = 0.25, \quad \gamma_2 = 1.875$.

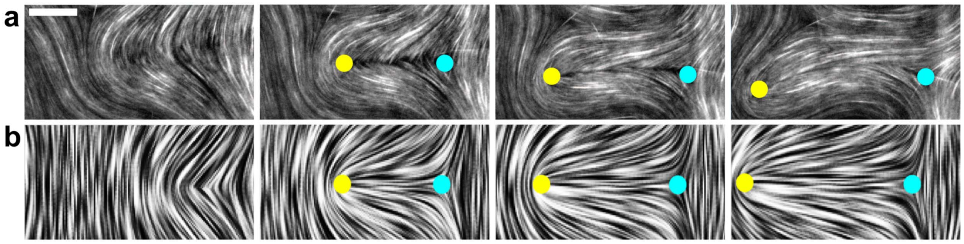

Figure 4. Defect-pair creation and propagation in experiment and theory. (a) Experimentally observed dynamics of a defect pair, spontaneously produced by buckling and subsequent fracture of filaments; adapted with permission from figure 3(d) in [5]. Scale bar 20 μm, time lapse 15 s. (b) Line integral convolution (LIC) plot of the director fields showing the spontaneous creation and propagation of a defect-pair in a simulation of equation (8) for $D = 1.5, \gamma_2 = 1$. As in the experiments, $+\frac{1}{2}$-defects (yellow) generally move faster than $-\frac{1}{2}$-defects (light blue), see figure 7.

Spontaneous defect-pair creation and subsequent propagation, as reported in recent ALC experiments [5] and observed in our simulations, are compared in figure 4. In the experimental system [5], a $\left(+\frac{1}{2}, -\frac{1}{2}\right)$-defect pair is created when fracture along incipient crack regions [20] becomes energetically more favorable than buckling. After creation, the $+\frac{1}{2}$-defect moves away rapidly whereas the position of the $-\frac{1}{2}$-defect remains approximately fixed for up to several seconds (figure 4(a)). We note that an asymmetry in the speeds of topological defects has also been observed in passive liquid crystals [77–79]. Our simulations of the minimal model defined in equation (8) accurately reproduce the details of the experimentally observed dynamics (figure 4(b); Movies S1 and S2).

Another striking and unexplained experimental observation [48] is the emergence of orientational order of $+\frac{1}{2}$-defects in thin ALC layers (figure 5). Using the setup illustrated in figure 1(b), recent experiments [48] demonstrated nematic alignment of $+\frac{1}{2}$-defects in thin ALC layers of thickness $h \sim 250$ nm (figure 5(a)), whereas thicker ALC layers with $h \sim 1\ \mu$m showed no substantial orientational order on large scales (figure 5(b)). To investigate whether our theory can account for these phenomena, we tracked defect positions $\boldsymbol{r}_i$ (Methods) and defect orientations $\boldsymbol{d}_i = \nabla \cdot Q(\boldsymbol{r}_i)/|\nabla \cdot Q(\boldsymbol{r}_i)|$ [80] in simulations for different values of the advection parameter $D = \zeta/\nu$, since Brinkman-type scaling arguments suggest that D increases with the ALC layer thickness, $D \propto 1/\nu \propto h^p$ with $p \in [1, 2]$. For weakly supercritical advection, $D \gtrsim D_c$, we find that equation (8) predicts robust antipolar alignment of $+\frac{1}{2}$-defects (figure 5(c)). In our simulations, this ordering decreases as the effective mixing strength D increases (figure 5(d)), consistent with the experimental results [48] for thicker ALC layers (figure 5(b)). Similar ordering was observed in simulations that incorporated alignment of the nematic field near the horizontal boundaries of the simulation box (supplementary information; figure S5). To quantify the degree of orientational order, we recorded the distances d_{ij} between all $+\frac{1}{2}$-defect pairs (i, j) as well as their relative orientation angles $\theta_{ij} = \cos^{-1}(\boldsymbol{d}_i \cdot \boldsymbol{d}_j) \in [0, \pi]$. The resulting pair-orientation distributions $p(\theta|r)$, and polar and nematic correlation functions, $P(r) = \langle \boldsymbol{d}_i \cdot \boldsymbol{d}_j \rangle_r$ and $N(r) = 2\langle (\boldsymbol{d}_i \cdot \boldsymbol{d}_j)^2 \rangle_r - 1$, are shown in figure 6, with $\langle \cdot \rangle_r$ denoting an average over pairs of defects separated by

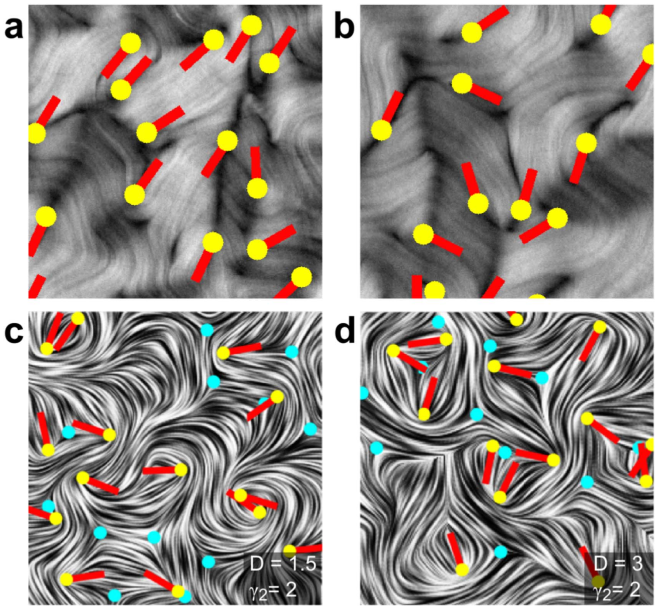

Figure 5. Strong and weak antipolar ordering of $+\frac{1}{2}$-defects as (a), (b) observed in experiments [48] and (c), (d) predicted by our theory based on 2D simulations with periodic boundary conditions. Light-blue markers: $-\frac{1}{2}$-defects. Yellow markers: $+\frac{1}{2}$-defects. Red bars: orientation of $+\frac{1}{2}$-defects. (a) $+\frac{1}{2}$-defects in thin ALC films (thickness $h\sim 250$ nm) show strong nematic alignment. (b) $+\frac{1}{2}$-defects in thicker ALC films ($h\sim 1\ \mu$m) are more disordered. (c), (d) For weak effective hydrodynamic coupling D, simulations show antipolar ordering, which is inhibited for larger values of D. The average number of defects in the full simulation box is approximately (c) 240 and (d) 350. Figures (a) and (b) kindly provided by DeCamp and Dogic.

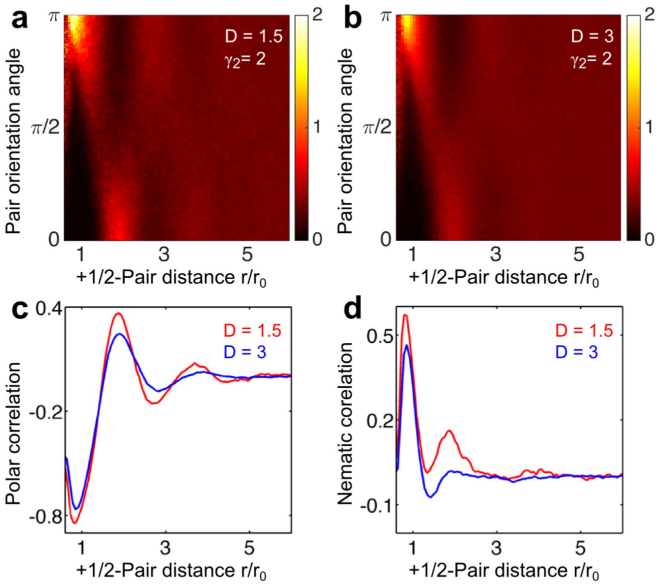

Figure 6. Increasing activity and film thickness decreases antipolar ordering in simulations. (a), (b) Maxima of the numerically obtained local pair orientation PDFs $p(\theta_{ij}|r)$ signal antipolar local ordering of $+\frac{1}{2}$-defects as they are separated by the typical defect-lattice spacing. The defect distance r is specified in units of the mean nearest-neighbor distance r_0 between $+\frac{1}{2}$-defects. (c), (d) Polar $P(r)$ and nematic $N(r)$ correlation functions for $D = 1.5$ (red) and $D = 3$ (blue). Increasing the effective hydrodynamic coupling D leads to stronger mixing and hence decreases nematic order, which is corroborated by the nematic correlation length being ∼40% shorter for $D = 3$ than for $D = 1.5$ (panel (d)). This is also reflected by the diminished intensity of the maxima in panel (b) relative to panel (a). The simulation parameters correspond to those given in figures 5(c) and (d).

a distance r. The local maxima in the orientation distribution at $\theta = 0$ and $\theta = \pi$ signal antipolar ordering (figure 6(a)), which is also reflected in the oscillatory behavior of the polar and nematic correlation functions (figures 6(c) and (d)). The diminished intensity of the local maxima for larger values of D indicates that enhanced hydrodynamic mixing reduces orientational order (figures 6(c) and (d)).

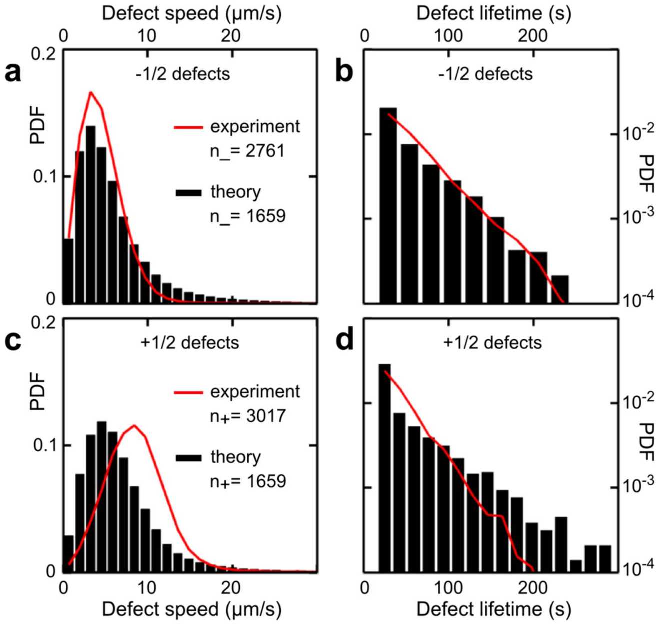

Figure 7. Quantitative comparison of defect statistics between predictions of equation (8) and experimental data [48], using the parameter estimation procedure described in the text. For $-\frac{1}{2}$-defects, both (a) speed distribution and (b) lifetime distribution agree well. (c) For $+\frac{1}{2}$-defects, experimentally measured speed values are slightly larger, as our model assumes a strongly overdamped limit. (d) Simulations with periodic boundary conditions (Movie S8) predict a low-probability tail of large lifetimes which is not visible in the experiment, likely due to its restricted field of view or additional noise. Dimensionless simulation parameters $D = 1.75$ and $\gamma_2 = 1$ translate into the following dimensional values: $a = 0.08\ \mathrm{s}^{-1}$, $b = 0.32\ \mathrm{s}^{-1}$, $D = 1791\ \mu\mathrm{m}^2\ \mathrm{s}^{-1}$, $\gamma_2 = 1024\ \mu\mathrm{m}^2\ \mathrm{s}^{-1}$, $\gamma_4 = 3.28 \times 10^6\ \mu\mathrm{m}^4\ \mathrm{s}^{-1}$. The numbers $n_\pm$ reflect the number of $\pm\frac{1}{2}$-defects tracked, and the simulation domain contained ~130 defects at any given time.

Lastly, we test the theoretically predicted defect statistics against a separate experimental data set kindly provided by DeCamp *et al* (private communication). Since our simulations are performed in dimensionless units, there is freedom to choose a characteristic lengthscale l_0 and timescale t_0. To relate theory and experiments, we determine $(l_0,\ t_0)$ such that the joint mean speed and mean lifetime of $\pm\frac{1}{2}$-defects match the experimental values $\bar{v} = 6.6\ \mu\mathrm{m\ s}^{-1}$ and $\bar{\tau} = 52.8$ s. After fixing these global scales, we can compare details of the speed and lifetime distributions (figure 7). To this end, we first locate the 'best-fit' simulation parameters in the $(\gamma_2,\ D)$-parameter space explored in the phase diagram (figure 2(a)). This procedure identifies $\gamma_2 = 1,\ D = 1.75$ as the best-match parameters, although nearby parameter values and simulations with $\kappa = 1$ produce fits of similar quality, corroborating the robustness of the model (figure S4). For $-\frac{1}{2}$-defects, we find adequate agreement between experiment and theory for speed and lifetime probability density functions (PDFs), as evident from figures 7(a) and (b). For $+\frac{1}{2}$-defects, simulation results also agree well with the experimental measurements (figures 7(c) and (d)), but one notices two systematic differences. First, while the peak heights of the PDFs agree within a few percent, experimentally measured speed values for $+\frac{1}{2}$-defects are on average slightly larger than theoretically predicted values (figure 7(c)). Second, simulation data predict a miniscule tail-fraction of long-living $+\frac{1}{2}$-defects not detected in the experiment (figure 7(d)). In addition, based on the experimental density estimate of 30 defects mm^{-2} [48], we find that the defect density at any given time in the 'best-fit' simulation is ~2.3× lower than in the experiments. As discussed below, such deviations can be explained plausibly by specific model assumptions. Taken together, the above results confirm that the minimal model defined by equation (8) provides a satisfactory qualitative and quantitative description of the main experimental results [5, 48].

Discussion

Pattern-formation mechanism

Equations (2) and (7) epitomize the idea of 'universality' in spatio-temporal pattern formation, as known from Swift–Hohenberg-type scalar field theories [53, 81]. The free-energy expressions contain the leading-order terms of generic series expansions in both order-parameter space and Fourier space, consistent with spatial and nematic symmetries. When considering passive systems with a preference for homogenization ($\gamma_2 < 0$), it usually suffices to keep only the quadratic gradient terms. By contrast, for pattern forming systems, the coefficient in front of the lowest-order gradient contribution can change sign [52, 53], and one must include higher-order derivatives to ensure stability. We hypothesize that the sign change of γ_2 is directly related to the motor-induced buckling of microtubule bundles (figure 1(a)), an effect that is not captured by the standard LdG free-energy for passive liquid crystals. In a few select cases, expressions of the form (2) and (7) can be systematically derived [52, 53, 82]. Generally, one can regard the free-energy expansion (7) as an effective field theory whose phenomenological parameters can be determined from experiments. This approach has proved successful for dense bacterial suspensions [15, 41] and now also for ALCs, indeed suggesting some universality in the formation and dynamics of topological defects in active systems.

Nematic defect order

Although (γ_2, D) are varied as independent effective parameters in the simulations, they are likely coupled through underlying physical and chemical parameters. For example, it is plausible that a change in ATP-concentration or film thickness would affect both γ_2 and D. The parameter D can also be interpreted as an effective Reynolds number. In our numerical exploration of the (γ_2, D)-parameter space, we observe for subcritical advection D either long-lived lattice-like states exhibiting nematically aligned $+\frac{1}{2}$-defects or defect-free ground-states (figures 2 and 3; Movies S3, S4, S5, S6 and S7). Ordered defect configurations correspond to local minima or saddles in the free-energy landscape and have only slightly higher energy than defect-free states (figure 2(c)). When the activity ζ is sufficiently large that advection is marginally supercritical, $D \gtrsim D_c$, chaotic system trajectories spend a considerable time in the vicinity of these metastable lattice states, which provides a physical basis for the orientational order of defects in thin ALC films [48]. For $D \gg D_c$, the ALC system can access a wider range of high-energy states, leading to increased disorder in the defect dynamics. Although the strongly turbulent regime $D \gg D_c$ requires high time-resolution and is thus difficult to realize in long-time simulations, the inhibition of nematic defect order at larger values of D is evident from the reduced peak heights in figures 6(c) and (d).

Defect statistics

The systematic speed deficit in figure 7(c) likely reflects the overdamped closure condition (4), which suppresses the propagation of hydrodynamic excitations. Since flow in a newly created defect pair generally points from the $-\frac{1}{2}$ to the $+\frac{1}{2}$-defect, the minimal model (8) can be expected to underestimate the speeds of $+\frac{1}{2}$-defects. This effect could be explored in future experiments through a controlled variation of the thickness and viscosity of the oil film (figure 1(b)). The low-probability tail of long-living $+\frac{1}{2}$-defects in the simulation data (figure 7(d)) may be due to the fact that they can be tracked indefinitely in the simulations but are likely to leave the finite field of view in the experiments. In the future, the minimal theory presented here should be extended systematically by adding physically permissible extra terms [83] to the free-energy, explicitly simulating the full hydrodynamics in equation (3), or incorporating additional terms into equation (1) that account for the interaction between the nematic field and the induced flow [65, 83].

Future extensions

The minimal model formulated in equations (1) and (2) can be systematically extended to improve further the quantitative agreement between experiment and theory. For instance, one may append to the right-hand side of (1) an additional fourth-order linear term of the form $(\nabla\nabla)^+[\nabla \cdot (\nabla \cdot Q)]$ [84], $\mathcal{O}^+$ denoting the symmetric traceless part of the operator $\mathcal{O}$. Such a term only affects the high-wavenumber damping at order k^4 and thus is not expected to alter significantly the results obtained here. We also note that extra terms coupling the nematic field to the induced flow may be added to equation (1), an example being SE, where $E = (1/2)[\nabla \boldsymbol{v} + (\nabla \boldsymbol{v})^\top]$ is the symmetrized strain rate tensor [25, 65]. Our above analysis neglected such secondary hydrodynamic effects in the interest of constructing a minimal mathematical theory capable of capturing key experimental observations. Moreover, this simplification may be justified on the physical basis that steric interactions and motor-induced buckling are expected to dominate over flow-alignment effects at high microtubule densities[3]. The effect of microtubule bending may be enhanced by appending a hydrodynamic interaction term proportional to E^+ [25], since the closure condition $\boldsymbol{v} = -D\nabla \cdot Q$ implies that $E^+ = -(D/2)\Delta Q$, which augments the bending term $-\gamma_2 \Delta Q$ in equation (2). However, the scale separation between the experimentally observed filament buckling wavelength and the flow structures in the isotropic phase at low microtubule concentrations (see figure 1(d) in [5]) suggests that such hydrodynamic effects play a secondary role. A natural next step would be to derive systematically the bending term from a microscopic model of motors and filaments as introduced in [20]. Finally, it will be worthwhile to attempt constructing a fully 3D theory for the ALCs and

---

[3] In active nematics of low to intermediate density, concentration fluctuations can trigger additional instabilities [85].

fluid and subsequently project on the quasi-2D interface, although additional assumptions are required then to obtain a closed 2D system of equations.

Conclusions

Recent experimental and theoretical studies showed that fourth-order PDE models for scalar and vector fields provide an accurate quantitative description of surface-pattern formation in soft elastic materials [52] and orientational order in dense bacterial fluids [15, 41]. Here, we have generalized these ideas to matrix-valued fields describing soft active nematics. The above analysis demonstrates that a generic fourth-order Q-tensor model can shed light on experimental observations in 2D ALCs [48], including the emergence of orientational order of topological defects. Physically, the higher-order generalization (2) becomes necessary because the commonly adopted LdG free-energy, which was designed to describe passive liquid crystals, does not account for the experimentally observed spontaneous buckling of motor-driven ALCs [5]. More generally, the fact that three vastly different soft matter systems can be treated quantitatively in terms of structurally similar higher-order PDEs [15, 41, 52] promises a unified mathematical framework for the description of pattern formation processes in a broad class of complex materials. In addition, the free-energy analogy [54] between dense ALCs and generalized Gross–Pitaevskii models suggests that the self-organization principles [40] of mesoscopic active matter and microscopic quantum systems [57–60] could be more similar than previously thought.

Methods

Numerical solver and defect tracking

To simulate equation (8), we implemented a numerical algorithm that evolves the real and imaginary parts $\lambda(t,\, \boldsymbol{r})$ and $\mu(t,\, \boldsymbol{r})$ of the complex order parameter ψ in time for periodic boundary conditions in space. The algorithm solves equation (8) pseudospectrally in space using $N_\ell = 256$ or $N_\ell = 512$ lattice points in each direction and a simulation box of size $L = 6\pi$ (figures 2 and 4) or $L = 18\pi$ (figures 3, 5–7). Spectral analysis shows that $N_\ell = 256$ is generally sufficient to resolve the fine-structure of the numerical solutions (supplementary figure S6). The algorithm steps forward in time using a modified exponential time-differencing fourth-order Runge–Kutta method [76] with time step $\Delta t \leqslant 2^{-10}$. Simulations were initialized with either a single defect pair or random field configurations $\{\lambda(0,\, \boldsymbol{r}),\ \mu(0,\, \boldsymbol{r})\}$. Defects are located at the intersections of the zero-contours of λ and μ, their positions tracked by implementing James Munkres' variant of the Hungarian assignment algorithm [86] (supplementary information).

Acknowledgments

This work was supported by the NSF Mathematical Sciences Postdoctoral Research Fellowship DMS-1400934 (AO), an MIT Solomon Buchsbaum Fund Award (J D) and an Alfred P Sloan Research Fellowship (JD). The authors would like to thank Zvonimir Dogic and Stephen DeCamp for sharing their experimental data and explaining the details of their experiments, and Hugues Chaté, Michael Hagan, Jean-François Joanny, Ken Kamrin, Mehran Kardar, Cristina Marchetti, Jonasz Slomka, Norbert Stoop, Francis Woodhouse and Martin Zwierlein for insightful discussions and helpful comments.

References

[1] McEvoy M A and Correll N 2015 Materials that couple sensing, actuation, computation, and communication *Science* **347** 6228
[2] Douglas S M, Marblestone A H, Teerapittayanon S, Vazquez A, Church G M and Shih W M 2009 Rapid prototyping of 3D DNA-origami shapes with caDNAno *Nucl. Acids Res.* **37** 5001–6
[3] Schaller V, Weber C, Semmrich C, Frey E and Bausch A R 2010 Polar patterns of driven filaments *Nature* **467** 73–7
[4] Sumino Y, Nagai K H, Shitaka Y, Tanaka D, Yoshikawa K, Chaté H and Oiwa K 2012 Large-scale vortex lattice emerging from collectively moving microtubules *Nature* **483** 448–52
[5] Sanchez T, Chen D T N, DeCamp S J, Heymann M and Dogic Z 2012 Spontaneous motion in hierarchically assembled active matter *Nature* **491** 431
[6] Rothemund P W K 2006 Folding DNA to create nanoscale shapes and patterns *Nature* **440** 297–302
[7] Nickels P C, Ke Y, Jungmann R, Smith D M, Leichsenring M, Shih W M, Liedl T and Høgberg B 2014 DNA origami structures directly assembled from intact bacteriophages *Small* **10** 1765–9
[8] Studart A R and Erb R M 2014 Bioinspired materials that self-shape through programmed microstructures *Soft Matter* **10** 1284–94
[9] Toner J and Tu Y 1998 Flocks, herds, and schools: a quantitative theory of flocking *Phys. Rev.* E **58** 4828–58
[10] Simha R A and Ramaswamy S 2002 Hydrodynamic fluctuations and instabilities in ordered suspensions of self-propelled particles *Phys. Rev. Lett.* **89** 058101
[11] Saintillan D and Shelley M 2008 Instabilities, pattern formation and mixing in active suspensions *Phys. Fluids* **20** 123304
[12] Giomi L, Mahadevan L, Chakraborty B and Hagan M F 2011 Excitable patterns in active nematics *Phys. Rev. Lett.* **106** 218101

[13] Peruani F, Ginelli F, Bär M and Chaté H 2011 Polar versus apolar alignment in systems of polar self-propelled particles *J. Phys.: Conf. Ser.* **297** 012014

[14] Peshkov A, Aranson I S, Bertin E, Chaté H and Ginelli F 2012 Nonlinear field equations for aligning self-propelled rods *Phys. Rev. Lett.* **109** 268701

[15] Wensink H H, Dunkel J, Heidenreich S, Drescher K, Goldstein R E, Löwen H and Yeomans J M 2012 Meso-scale turbulence in living fluids *Proc. Natl Acad. Sci. USA* **109** 14308–13

[16] Wensink H H and Löwen H 2012 Emergent states in dense systems of active rods: from swarming to turbulence *J. Phys. Condens. Matter* **24** 464130

[17] Ravnik M and Yeomans J M 2013 Confined active nematic flow in cylindrical capillaries *Phys. Rev. Lett.* **110** 026001

[18] Adhyapak T C, Ramaswamy S and Toner J 2013 Live soap: stability, order, and fluctuations in apolar active smectics *Phys. Rev. Lett.* **110** 118102

[19] Marchetti M C, Joanny J F, Ramaswamy S, Liverpool T B, Prost J, Rao M and Simha R A 2013 Hydrodynamics of soft active matter *Rev. Mod. Phys.* **85** 1143

[20] Gao T, Blackwell R, Glaser M A, Betterton M D and Shelley M J 2015 Multiscale polar theory of microtubule and motor-protein assemblies *Phys. Rev. Lett.* **114** 048101

[21] Giomi L 2015 Geometry and topology of turbulence in active nematics *Phys. Rev.* X **5** 031003

[22] Krieger M S, Spagnolie S E and Powers T R 2015 Microscale locomotion in a nematic liquid crystal *Soft Matter* **11** 9115–25

[23] Trivedi R R, Maeda R, Abbott N L, Spagnolie S E and Weibel D B 2015 Bacterial transport of colloids in liquid crystalline environments *Soft Matter* **11** 8404–8

[24] Menzel A M, Saha A, Hoell C and Löwen H 2016 Dynamical density functional theory for microswimmers *J. Chem. Phys.* **144** 024115

[25] Putzig E, Redner G, Baskaran A and Baskaran A 2016 Instabilities, defects, and defect ordering in an overdamped active nematic *Soft Matter* **12** 3854–9

[26] Doostmohammadi A, Adamer M F, Thampi S P and Yeomans J M 2016 Stabilization of active matter by flow-vortex lattices and defect ordering *Nat. Commun.* **7** 10557

[27] Mirkin C A, Letsinger R L, Mucic R C and Storhoff J J 1996 A DNA-based method for rationally assembling nanoparticles into macroscopic materials *Nature* **382** 607–9

[28] Valignat M-P, Theodoly O, Crocker J C, Russel W B and Chaikin P M 2005 Reversible self-assembly and directed assembly of DNA-linked micrometer-sized colloids *Proc. Natl Acad. Sci. USA* **102** 4225–9

[29] Palacci J, Sacanna S, Steinberg A P, Pine D J and Chaikin P M 2013 Living crystals of light-activated colloidal surfers *Science* **339** 936–40

[30] Ebeling W, Engel A and Feistel R 1992 *Physik der Evolutionsprozesse* (Berlin: Akademie Verlag)

[31] Zeravcic Z and Brenner M P 2014 Self replicating colloidal clusters *Proc. Natl Acad. Sci. USA* **111** 1748–53

[32] England J L 2013 Statistical physics of self-replication *J. Chem. Phys.* **139** 121923

[33] Berger B, Shor P W, Tucker-Kellogg L and King J 1994 Local rule-based theory of virus shell assembly *Proc. Natl Acad. Sci. USA* **91** 7732–6

[34] Perlmutter J D and Hagan M F 2015 Mechanisms of virus assembly *Annu. Rev. Phys. Chem.* **66** 217–39

[35] Meng G, Paulose J, Nelson D R and Manoharan V N 2014 Elastic instability of a crystal growing on a curved surface *Science* **343** 634–7

[36] Baskaran A and Marchetti M C 2008 Hydrodynamics of self-propelled hard rods *Phys. Rev.* E **77** 011920

[37] Baskaran A and Marchetti M C 2009 Statistical mechanics and hydrodynamics of bacterial suspensions *Proc. Natl Acad. Sci.* **106** 15567–72

[38] Vicsek T and Zafeiris A 2012 Collective motion *Phys. Rep.* **517** 71–140

[39] Ramaswamy S 2010 The mechanics and statistics of active matter *Annu. Rev. Cond. Mat. Phys.* **1** 323–45

[40] Goldenfeld N and Woese C 2011 Life is physics: evolution as a collective phenomenon far from equilibrium *Annu. Rev. Cond. Mat. Phys.* **2** 375–99

[41] Dunkel J, Heidenreich S, Drescher K, Wensink H H, Bär M and Goldstein R E 2013 Fluid dynamics of bacterial turbulence *Phys. Rev. Lett.* **110** 228102

[42] Weber C A, Hanke T, Deseigne J, Léonard S, Dauchot O, Frey E and Chaté H 2013 Long-range ordering of vibrated polar disks *Phys. Rev. Lett.* **110** 208001

[43] Suzuki R, Weber C A, Frey E and Bausch A 2015 Polar pattern formation in driven filament systems requires non-binary particle collisions *Nat. Phys.* **11** 839–43

[44] Narayan V, Ramaswamy S and Menon N 2007 Long-lived giant number fluctuations in a swarming granular nematic *Science* **317** 105–8

[45] Aranson I S, Snezhko A, Olafsen J S and Urbach J S 2008 Comment on 'long-lived giant number fluctuations in a swarming granular nematic' *Science* **320** 612

[46] Shi X-Q and Ma Y-Q 2013 Topological structure dynamics revealing collective evolution in active nematics *Nat. Commun.* **4** 3013

[47] Keber F C, Loiseau E, Sanchez T, DeCamp S J, Giomi L, Bowick M J, Marchetti M C, Dogic Z and Bausch A R 2014 Topology and dynamics of active nematic vesicles *Science* **345** 1135–9

[48] DeCamp S J, Redner G S, Baskaran A, Hagan M F and Dogic Z 2015 Orientational order of motile defects in active nematics *Nat. Mater.* **14** 1110–5

[49] Musevic I, Skarabot M, Tkalec U, Ravnik M and Zumer S 2006 Two-dimensional nematic colloidal crystals self-assembled by topological defects *Science* **313** 954–8

[50] Machon T and Alexander G P 2013 Knots and nonorientable surfaces in chiral nematics *Proc. Natl Acad. Sci. USA* **110** 14174–9

[51] Tkalec U, Ravnik M, Copar S, Zumer S and Musevic I I 2011 Reconfigurable knots and links in chiral nematic colloids *Science* **333** 62–5

[52] Stoop N, Lagrange R, Terwagne D, Reis P M and Dunkel J 2015 Curvature-induced symmetry breaking determines elastic surface patterns *Nat. Mater.* **14** 337–42

[53] Swift J and Hohenberg P C 1977 Hydrodynamic fluctuations at the convective instability *Phys. Rev.* A **15** 319–28

[54] Renn S R and Lubensky T C 1988 Abrikosov dislocation lattice in a model of the cholesteric-to-smectic-A transition *Phys. Rev.* A **38** 2132–47

[55] Gross E P 1961 Structure of a quantized vortex in boson systems *Nuovo Cim.* **20** 454–77

[56] Pitaevskii L P 1961 Vortex lines in an imperfect Bose gas *Sov. Phys.—JETP* **13** 451–4

[57] Higbie J and Stamper-Kurn D M 2002 Periodically dressed Bose–Einstein condensate: a superfluid with an anisotropic and variable critical velocity *Phys. Rev. Lett.* **88** 090401

[58] Lin Y J, Jimenez-Garcia K and Spielman I B 2011 Spin–orbit-coupled Bose–Einstein condensates *Nature* **471** 83–6

[59] Cheuk L W, Sommer A T, Hadzibabic Z, Yefsah T, Bakr W S and Zwierlein M W 2012 Spin-injection spectroscopy of a spin–orbit coupled Fermi gas *Phys. Rev. Lett.* **109** 095302

[60] Parker C V, Ha L-C and Chin C 2013 Direct observation of effective ferromagnetic domains of cold atoms in a shaken optical lattice *Nat. Phys.* **9** 769–74

[61] de Gennes P G 1972 An analogy between superconductors and smectics A *Solid State Commun.* **10** 753–6

[62] Goodby J W, Waugh M A, Stein S M, Chin E, Pindak R and Patel J S 1989 Characterization of a new helical smectic liquid crystal *Nature* **337** 449–552

[63] Srajer G, Pindak R, Waugh M A and Goodby J W 1990 Structural measurements on the liquid–crystal analog of the Abrikosov phase *Phys. Rev. Lett.* **64** 1545–8

[64] Thampi S P, Golestanian R and Yeomans J M 2013 Velocity correlations in an active nematic *Phys. Rev. Lett.* **111** 118101

[65] Giomi L, Bowick M J, Ma X and Marchetti M C 2013 Defect annihilation and proliferation in active nematics *Phys. Rev. Lett.* **110** 228101

[66] Sokolov A, Aranson I S, Kessler J O and Goldstein R E 2007 Concentration dependence of the collective dynamics of swimming bacteria *Phys. Rev. Lett.* **98** 158102

[67] Kraichnan R H and Montogomery D 1980 Two-dimensional turbulence *Rep. Prog. Phys.* **43** 547–619

[68] Kellay H and Goldburg W I 2002 Two-dimensional turbulence: a review of some recent experiments *Rep. Prog. Phys.* **65** 845–94

[69] de Gennes P G and Prost J 1995 *The Physics of Liquid Crystals* vol 2 (Oxford: Oxford University Press)

[70] Vetter R, Stoop N, Wittel F K and Herrmann H J 2014 Simulating thin sheets: buckling, wrinkling, folding and growth *J. Phys.: Conf. Ser.* **487** 012012

[71] Haghpanah B, Papadopoulos J, Mousanezhad D, Nayeb-Hashemi H and Vaziri A 2014 Buckling of regular, chiral and hierarchical honeycombs under a general macroscopic stress state *Proc. R. Soc.* A **470** 20130856

[72] Kang S H, Shan S, Košmrlj A, Noorduin W L, Shian S, Weaver J C, Clarke D R and Bertoldi K 2014 Complex ordered patterns in mechanical instability induced geometrically frustrated triangular cellular structures *Phys. Rev. Lett.* **112** 098701

[73] Evans E and Sackmann E 1988 Translational and rotational drag coefficients for a disk moving in a liquid membrane associated with a rigid substrate *J. Fluid Mech.* **194** 553–61

[74] Woodhouse F G and Goldstein R E 2013 Cytoplasmic streaming in plant cells emerges naturally by microfilament self-organization *Proc. Natl Acad. Sci. USA* **110** 14132–7

[75] Voituriez R, Joanny J F and Prost J 2006 Generic phase diagram of active polar films *Phys. Rev. Lett.* **96** 028102

[76] Kassam A-K and Trefethen L N 2005 Fourth-order time-stepping for stiff PDEs *SIAM J. Sci. Comput.* **26** 1214–33

[77] Tóth G, Denniston C and Yeomans J M 2002 Hydrodynamics of topological defects in nematic liquid crystals *Phys. Rev. Lett.* **88** 105504

[78] Švensek D and Žumer S 2002 Hydrodynamics of pair-annihilating disclination lines in nematic liquid crystals *Phys. Rev.* E **66** 021712

[79] Blanc C, Švensek D, Žumer S and Nobili M 2005 Dynamics of nematic liquid crystal disclinations: the role of backflow *Phys. Rev. Lett.* **95** 097802

[80] Vromans A J and Giomi L 2016 Orientational properties of nematic disclinations *Soft Mat.* **12** 6490–5

[81] Aranson I S and Tsimring L S 2006 Patterns and collective behavior in granular media: theoretical concepts *Rev. Mod. Phys.* **78** 641–92

[82] Großmann R, Romanczuk P, Bär M and Schimansky-Geier L 2014 Vortex arrays and mesoscale turbulence of self-propelled particles *Phys. Rev. Lett.* **113** 258104

[83] Stark H and Lubensky T C 2003 Poisson-bracket approach to the dynamics of nematic liquid crystals *Phys. Rev.* E **67** 061709

[84] Bertin E, Chaté H, Ginelli F, Mishra S, Peshkov A and Ramaswamy S 2013 Mesoscopic theory for fluctuating active nematics *New J. Phys.* **15** 05032

[85] Ngo S, Peshkov A, Aranson I S, Bertin E, Ginelli F and Chaté H 2014 Large-scale chaos and fluctuations in active nematics *Phys. Rev. Lett.* **113** 038302

[86] Munkres J 1957 Algorithms for assignment and transportation problems *J. Soc. Indust. Appl. Math.* **5** 32–8

Supplementary Information:
Antipolar ordering of topological defects in active liquid crystals

Anand U. Oza[1] and Jörn Dunkel[2]
[1] *Courant Institute of Mathematical Sciences, New York University, 251 Mercer Street, New York, NY 10012, USA*
[2] *Department of Mathematics, Massachussetts Institute of Technology,*
77 Massachusetts Avenue, Cambridge, MA 02139-4307, USA

(Dated: August 23, 2016)

ADVECTION TERM IN GOVERNING EQUATION

We here motivate the form of the advection term $\nabla \cdot (\boldsymbol{v}Q)$ in Eq. (1) of the Main Text. Let $\mathcal{P} = \mathcal{P}(t, \boldsymbol{r}, \boldsymbol{p})$ denote the probability density function of active liquid crystal positions $\boldsymbol{r}$ and orientations $\boldsymbol{p}$, the latter being a unit vector. The conservation law for $\mathcal{P}$ assumes the form

$$\partial_t \mathcal{P} = -\nabla_{\boldsymbol{r}} \cdot \boldsymbol{j}_{\boldsymbol{r}} - \nabla_{\boldsymbol{p}} \cdot \boldsymbol{j}_{\boldsymbol{p}}, \tag{1}$$

where $\boldsymbol{j}_{\boldsymbol{r}}$ and $\boldsymbol{j}_{\boldsymbol{p}}$ are the position and orientation fluxes, respectively. Since the ALCs are advected with the fluid, the position flux has the form

$$\boldsymbol{j}_{\boldsymbol{r}} = \boldsymbol{v}\mathcal{P} + \ldots, \tag{2}$$

where $\boldsymbol{v} = \boldsymbol{v}(t, \boldsymbol{r})$ is the local fluid velocity and the '$\ldots$' stand for additional translational diffusive and interaction contributions. Multiplying both sides of (1) by $\boldsymbol{pp}$ and integrating with respect to $\boldsymbol{p}$, we obtain an equation of the form

$$\partial_t \overline{\boldsymbol{pp}} = -\nabla_{\boldsymbol{r}} \cdot (\boldsymbol{v}\overline{\boldsymbol{pp}}) + \ldots, \tag{3}$$

where

$$\overline{\boldsymbol{pp}}(t, \boldsymbol{r}) = \int_{|\boldsymbol{p}|=1} \mathrm{d}\boldsymbol{p}\, \mathcal{P}(\boldsymbol{x}, \boldsymbol{n}, t)\boldsymbol{pp} \tag{4}$$

is the second moment tensor of the local ALC orientations. Projecting on the traceless part of Eq. (3) and moving the advective term to the lhs. then gives

$$\partial_t Q + \nabla_{\boldsymbol{r}} \cdot (\boldsymbol{v}Q) = \ldots \tag{5}$$

for the nematic order parameter tensor Q.

As discussed in the Main Text, the simplification $\nabla_{\boldsymbol{r}} \cdot (\boldsymbol{v}Q) = \boldsymbol{v} \cdot \nabla_{\boldsymbol{r}} Q$ is not valid for compressible flow, for which $\nabla_{\boldsymbol{r}} \cdot \boldsymbol{v} \neq 0$ in general. Note that the contributions from the orientation flux $\boldsymbol{j}_{\boldsymbol{p}}$ lead to the free energy contributions, and possibly to additional non-potential terms depending on the details of the microscopic model, as has been shown for dry active matter [2]. However, they will not affect the advection term, as $\boldsymbol{j}_{\boldsymbol{p}}$ couples only through $\nabla_{\boldsymbol{p}}$ but not $\nabla_{\boldsymbol{x}}$. We have thus shown that the advection term $\nabla \cdot (\boldsymbol{v}Q)$ emerges naturally from a generic microscopic model of particles that are confined to a 2D surface (e.g., by surfactants imposing an effective trapping potential as in the experiments [1]) and transported by a compressible interfacial flow.

PARTIAL DIFFERENTIAL EQUATION AND NONDIMENSIONALIZATION

In this paper, we study the following partial differential equation for the nematic order tensor $Q(t, \boldsymbol{r})$:

$$\partial_t Q + \nabla \cdot (\boldsymbol{v}Q) - \kappa[Q, \omega] = -\frac{\delta \mathcal{F}}{\delta Q}, \tag{6}$$

where $\omega = \left(\nabla \boldsymbol{v} - (\nabla \boldsymbol{v})^T\right)/2$ is the vorticity tensor and $\boldsymbol{v} = -D\nabla \cdot Q$ the fluid velocity. The effective free energy $\mathcal{F}[Q] = \int \mathrm{d}^2 r\, F(Q)$ has density

$$F(Q) = \mathrm{Tr}\left\{-\frac{a}{2}Q^2 + \frac{b}{4}Q^4 - \frac{\gamma_2}{2}(\nabla Q)^2 + \frac{\gamma_4}{2}(\nabla\nabla Q)^2\right\}, \tag{7}$$

where $\mathrm{Tr}\{(\nabla Q)^2\} = (\partial_k Q_{ij})(\partial_k Q_{ij})$ and $\mathrm{Tr}\{(\nabla\nabla Q)^2\} = (\partial_k\partial_l Q_{ij})(\partial_k\partial_l Q_{ij})$, summation over repeated indices being implied. Abbreviating $\Delta = \nabla^2$, the variational derivative of F with respect to Q has the form

$$\begin{aligned}\frac{\delta\mathcal{F}}{\delta Q} &= -aQ + bQ^3 + \frac{\gamma_2}{2}\nabla\cdot\frac{\partial F}{\partial(\nabla Q)} + \frac{\gamma_4}{2}\nabla\cdot\left[\nabla\cdot\frac{\partial F}{\partial(\nabla\nabla Q)}\right]\\ &= -aQ + bQ^3 + \gamma_2\Delta Q + \gamma_4\Delta^2 Q \end{aligned}\tag{8}$$

from which we obtain the governing equation

$$\partial_t Q - D\nabla\cdot((\nabla\cdot Q)Q) - \kappa[Q,\omega] = aQ - bQ^3 - \gamma_2\Delta Q - \gamma_4\Delta^2 Q, \quad \boldsymbol{r}\in[0,L]^2. \tag{9}$$

In component form, we have $\omega_{ij} = (\partial_i v_j - \partial_j v_i)/2$ and $v_i = -D\partial_j Q_{ji}$ and so obtain

$$\begin{aligned}\partial_t Q_{ij} - D\partial_k\left(\left(\partial_l Q_{lk}\right)Q_{ij}\right) + \frac{\kappa D}{2}\left(Q_{ik}\partial_l\left(\partial_k Q_{lj} - \partial_j Q_{lk}\right) + Q_{kj}\partial_l\left(\partial_k Q_{li} - \partial_i Q_{lk}\right)\right)&\\ = aQ_{ij} - b(Q_{ij})^3 - \gamma_2\Delta Q_{ij} - \gamma_4\Delta^2 Q_{ij}.&\end{aligned}\tag{10}$$

We rescale Q according to $Q \to 2\sqrt{a/b}Q$, and define a characteristic length scale $L_c = (4a/\gamma_4)^{1/4}$ and time scale $T_c = 1/4a$. The dimensionless equation is thus

$$\partial_t Q - \tilde{D}\nabla\cdot((\nabla\cdot Q)Q) - \kappa[Q,\omega] = Q\left(\frac{1}{4} - Q^2\right) - \tilde{\gamma_2}\Delta Q - \Delta^2 Q, \quad \boldsymbol{r}\in[0,L/L_c]^2, \tag{11}$$

where $\tilde{D} = D/\sqrt{b\gamma_4}$ and $\tilde{\gamma_2} = \gamma_2/\sqrt{4a\gamma_4}$. In our simulations, we use $L/L_c = 2\pi N_\gamma$ where $3 \le N_\gamma \le 9$. Dropping the tildes and writing $Q = \begin{pmatrix}\lambda & \mu\\ \mu & -\lambda\end{pmatrix}$, we obtain the following equations for $\lambda(t,\boldsymbol{r})$ and $\mu(t,\boldsymbol{r})$:

$$\begin{aligned}\partial_t\lambda &= D\left(\lambda_x^2 - \lambda_y^2 + \lambda_x\mu_y + \lambda_y\mu_x\right) + D\left(\lambda_{xx} + 2\mu_{xy} - \lambda_{yy}\right)\lambda - \kappa D\left(\mu_{yy} + 2\lambda_{xy} - \mu_{xx}\right)\mu\\ &\quad + \lambda\left(\frac{1}{4} - \lambda^2 - \mu^2\right) - \gamma_2\Delta\lambda - \Delta^2\lambda\\ \partial_t\mu &= D\left(\lambda_x\mu_x - \lambda_y\mu_y + 2\mu_x\mu_y\right) + D\left(\lambda_{xx} + 2\mu_{xy} - \lambda_{yy}\right)\mu + \kappa D\left(\mu_{yy} + 2\lambda_{xy} - \mu_{xx}\right)\lambda\\ &\quad + \mu\left(\frac{1}{4} - \lambda^2 - \mu^2\right) - \gamma_2\Delta\mu - \Delta^2\mu\end{aligned}\tag{12}$$

In this paper, we restrict our attention to the regime $D, \kappa \ge 0$, corresponding to an extensile active liquid crystal. All variables are henceforth assumed to be dimensionless unless otherwise stated.

The nematic order parameter $S(t,\boldsymbol{r})$ and director $\boldsymbol{n}(t,\boldsymbol{r})$ may be written in terms of λ and μ as follows:

$$S = 2\sqrt{\lambda^2 + \mu^2}, \quad \boldsymbol{n} = \frac{1}{\sqrt{\left(\lambda + \frac{S}{2}\right)^2 + \mu^2}}\begin{pmatrix}\lambda + \frac{S}{2}\\ \mu\end{pmatrix}. \tag{13}$$

Note that S is twice the larger eigenvalue of Q, and $\boldsymbol{n}$ is the corresponding eigenvector.

LINEAR STABILITY ANALYSIS

We here consider the linear stability of the uniform state $\lambda = \frac{1}{2}\cos 2\theta$ and $\mu = \frac{1}{2}\sin 2\theta$, in which the nematic director field is uniformly aligned with fixed angle θ. Specifically, we substitute $\lambda = \frac{1}{2}\cos 2\theta + \epsilon\hat{\lambda}(t)\mathrm{e}^{i\boldsymbol{k}\cdot\boldsymbol{r}}$ and $\mu = \frac{1}{2}\sin 2\theta + \epsilon\hat{\mu}(t)\mathrm{e}^{i\boldsymbol{k}\cdot\boldsymbol{r}}$ into (12) and retain terms at order ϵ (dropping the hats):

$$\begin{aligned}\lambda_t &= \frac{D}{2}\cos 2\theta\left[-\lambda\cos 2\phi - \mu\sin 2\phi\right]k^2 - \frac{\kappa D}{2}\sin 2\theta\left[\mu\cos 2\phi - \lambda\sin 2\phi\right]k^2,\\ &\quad - \frac{1}{2}\cos 2\theta\left(\lambda\cos 2\theta + \mu\sin 2\theta\right) + (\gamma_2 k^2 - k^4)\lambda\\ \mu_t &= \frac{D}{2}\sin 2\theta\left[-\lambda\cos 2\phi - \mu\sin 2\phi\right]k^2 + \frac{\kappa D}{2}\cos 2\theta\left[\mu\cos 2\phi - \lambda\sin 2\phi\right]k^2\\ &\quad - \frac{1}{2}\sin 2\theta\left(\lambda\cos 2\theta + \mu\sin 2\theta\right) + (\gamma_2 k^2 - k^4)\mu,\end{aligned}\tag{14}$$

where $\boldsymbol{k} = k(\cos\phi, \sin\phi)$. This system of linear equations may be written in the form $\dot{\boldsymbol{\Psi}} = \boldsymbol{M}\boldsymbol{\Psi}$ where $\boldsymbol{\Psi} = (\lambda, \mu)$. The eigenvalues $\sigma_\pm$ of $\boldsymbol{M}$ are

$$\sigma_\pm(k,u) = \gamma_2 k^2 - k^4 - \frac{1}{4}\left[1 + (1-\kappa)Dk^2u \pm \sqrt{\left[1+(1+\kappa)Dk^2u\right]^2 + 4\kappa D^2k^4(1-u^2)}\right] \tag{15}$$

where $u = \cos[2(\phi - \theta)]$. Note that $\sigma_\pm \in \mathbb{R}$ and $\sigma_- > \sigma_+$, so the stability of the uniform state is determined by the wavenumber $k = k^*$ and angle $\phi = \phi^*$ for which $\sigma_-(k,u)$ is largest.

We begin by finding the value of u (or equivalently, ϕ) for which $\sigma_-(k,u)$ is largest for any fixed k. One can show that $\mathrm{d}\sigma_-/\mathrm{d}u \neq 0$ on the interval $-1 \le u \le 1$ for $\kappa > 0$, so σ_- must attain its maximum at $u = \pm 1$ for every k. Note that

$$\begin{aligned}
\sigma_-(k, u=1) &= \gamma_2 k^2 - k^4 - \frac{1}{4}\left[1 + (1-\kappa)Dk^2 - \left|1+(1+\kappa)Dk^2\right|\right] \\
&= \gamma_2 k^2 - k^4 + \frac{1}{2}\kappa D k^2 \quad \text{and} \\
\sigma_-(k, u=-1) &= \gamma_2 k^2 - k^4 - \frac{1}{4}\left[1 - (1-\kappa)Dk^2 - \left|1-(1+\kappa)Dk^2\right|\right] \\
&= \gamma_2 k^2 - k^4 - \frac{1}{2}\cdot\begin{cases} \kappa D k^2 & \text{if } k \le [(1+\kappa)D]^{-1/2} \\ 1 - Dk^2 & \text{otherwise} \end{cases},
\end{aligned} \tag{16}$$

so the difference is

$$\sigma_-(k,u=1) - \sigma_-(k,u=-1) = \frac{1}{2}\cdot\begin{cases} 2\kappa Dk^2 & \text{if } k \le [(1+\kappa)D]^{-1/2} \\ 1 + (\kappa-1)Dk^2 & \text{otherwise} \end{cases}. \tag{17}$$

This quantity is nonnegative if $0 \le \kappa < 1$ and $k \le k_c \equiv [(1-\kappa)D]^{-1/2}$, or if $\kappa \ge 1$. We thus obtain

$$\sigma_-^*(k) \equiv \max_{-1\le u\le 1} \sigma_-(k,u) = \gamma_2 k^2 - k^4 + \frac{1}{2}\cdot\begin{cases} \kappa Dk^2 & \text{for } u = 1 \text{ if } \kappa \ge 1 \\ \kappa Dk^2 & \text{for } u = u^* \text{ if } 0 \le \kappa < 1 \text{ and } k \le k_c \\ Dk^2 - 1 & \text{for } u = -1 \text{ if } 0 \le \kappa < 1 \text{ and } k > k_c \end{cases}, \tag{18}$$

where $u^* = 1$ for $0 < \kappa < 1$, and is arbitrary for $\kappa = 0$; indeed, $\sigma_-(k,u)$ is independent of u for $\kappa = 0$ and $k \le k_c$. We now need to find the wavenumber k for which $\sigma_-^*(k)$ is largest. To this end, we consider separately the cases $\gamma_2 > 0$ and $\gamma_2 < 0$.

Case 1: $\gamma_2 > 0$

For $\gamma_2 > 0$, note that the maxima of the functions obtained in (18) are

$$\begin{aligned}
r_1 &\equiv \max_{k\ge 0}\left[\left(\gamma_2 + \frac{\kappa D}{2}\right)k^2 - k^4\right] = \frac{1}{4}\left(\gamma_2 + \frac{\kappa D}{2}\right)^2 \quad \text{for} \quad k = k_1 \equiv \left[\frac{1}{2}\left(\gamma_2 + \frac{\kappa D}{2}\right)\right]^{1/2}, \\
r_2 &\equiv \max_{k\ge 0}\left[-\frac{1}{2} + \left(\gamma_2 + \frac{D}{2}\right)k^2 - k^4\right] = \frac{1}{2}\left[-1 + \frac{1}{2}\left(\gamma_2 + \frac{D}{2}\right)^2\right] \quad \text{for} \quad k = k_2 \equiv \left[\frac{1}{2}\left(\gamma_2 + \frac{D}{2}\right)\right]^{1/2}.
\end{aligned} \tag{19}$$

The system may thus undergo either of three instabilities: an *isotropic instability* in which the dominant instability is independent of the direction ϕ, a *longitudinal instability* in which the most unstable mode points along the nematic director field, or a *transverse instability* in which it points perpendicular to the nematic director field. The isotropic and longitudinal instabilities have growth rate r_1 corresponding to wavenumber $k^* = k_1$, the longitudinal mode having angle $\phi^* = \theta$. The transverse instability has growth rate r_2 corresponding to wavenumber $k^* = k_2$ and angle $\phi^* = \theta + \pi/2$. From (18), we conclude that the system undergoes a longitudinal instability for $\kappa \ge 1$.

The stability behavior for $0 < \kappa < 1$ is more complicated, as there are four possibilities to consider: (i) $k_2 < k_c$, (ii) $k_c < k_1$, (iii) $k_1 < k_c < k_2$ and $r_1 > r_2$, and (iv) $k_1 < k_c < k_2$ and $r_1 < r_2$. A longitudinal instability occurs in cases (i) and (iii), whereas a transverse instability occurs in cases (ii) and (iv). Note that

$$r_1 - r_2 = \frac{1}{2}\left[1 - \frac{(1-\kappa)D}{2}\left(\gamma_2 + \frac{(1+\kappa)D}{4}\right)\right] = \frac{1}{2}\left(1 - \frac{k_1^2 + k_2^2}{2k_c^2}\right), \tag{20}$$

so $r_1 > r_2$ is equivalent to $k_1^2 + k_2^2 < 2k_c^2$. Since $k_1 < k_2$ we conclude that we obtain a longitudinal instability in the parameter regime

$$\frac{(1-\kappa)D}{2}\left(\gamma_2 + \frac{(1+\kappa)D}{4}\right) < 1, \quad \text{or equivalently} \quad D < D_c \equiv \frac{2}{1+\kappa}\left(-\gamma_2 + \sqrt{\gamma_2^2 + \frac{2(1+\kappa)}{1-\kappa}}\right), \tag{21}$$

whereas we obtain a transverse instability in the regime $D > D_c$. If $D = D_c$, both instabilities have the same growth rate and thus are equally responsible for the destabilization of the uniformly aligned state.

For the special case $\kappa = 0$ considered in the main text, the system undergoes an isotropic instability for $D < D_c$, and a transverse instability otherwise. We may also simplify the above formulae: $D_c = 2\left(-\gamma_2 + \sqrt{\gamma_2^2 + 2}\right)$, $r_1 = \gamma_2^2/4$ and $k_1 = \sqrt{\gamma_2/2}$. The formulae for r_2 and k_2 remain unchanged.

Case 2: $\gamma_2 < 0$

An extension of the analysis in the previous section allows us to determine the stability properties of the uniformly aligned state in the parameter regime $\gamma_2 < 0$. The system may now exhibit one of four behaviors: an isotropic instability, a longitudinal instability, a transverse instability, or no instability at all, in which perturbations to the uniformly aligned state do not grow in time.

For $\kappa \geq 1$, we find that the uniform state undergoes a longitudinal instability if $D > 2|\gamma_2|/\kappa$ and is stable otherwise. For $0 \leq \kappa < 1$, the behavior is more complicated, but it is straightforward to use our analysis from the previous section, keeping in mind that the unstable wavenumbers k_1 and k_2 must be real. We find that the uniform state undergoes a longitudinal instability if $2|\gamma_2|/\kappa < D < D_c$, a transverse instability if $D > \max(2\left(|\gamma_2| + \sqrt{2}\right), D_c)$, and is stable otherwise.

It is interesting to note that, even in the parameter regime $\gamma_2 < 0$, the effect of hydrodynamics is sufficient to destabilize the uniform state, provided that the velocity coefficient D and vorticity coefficient κ are sufficiently large so as to overcome the stabilizing influence of the elastic coefficient γ_2. Specifically, for $\kappa \geq 1$, the uniform state undergoes an instability for $\frac{\kappa D}{2} > |\gamma_2|$. For $0 \leq \kappa < 1$, it destabilizes for $D > \min(2\left(|\gamma_2| + \sqrt{2}\right), 2|\gamma_2|/\kappa)$. The system dynamics for $\gamma_2 < 0$ will be considered in future work.

The results of the stability analysis are summarized in Fig. S1.

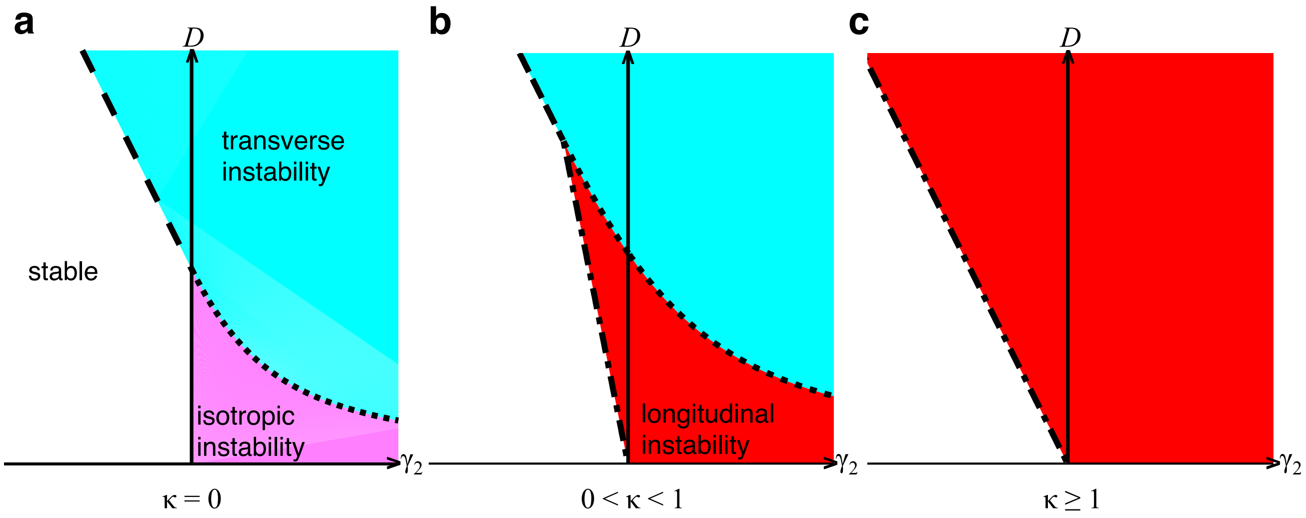

Fig. S1: Results of the linear stability analysis of the uniformly aligned state in the (γ_2, D) plane, for (**a**) $\kappa = 0$, (**b**) $0 < \kappa < 1$ and (**c**) $\kappa \geq 1$. The uniform state is stable in the white regions; it undergoes an isotropic instability in the pink region, a longitudinal instability along the director field in the red regions, and a transverse instability perpendicular to the director field in the blue regions. The dashed curve corresponds to $D = 2\left(|\gamma_2| + \sqrt{2}\right)$, the dotted curve to $D = D_c \equiv \frac{2}{1+\kappa}\left(-\gamma_2 + \sqrt{\gamma_2^2 + \frac{2(1+\kappa)}{1-\kappa}}\right)$, and the dashed-dotted curve to $D = 2|\gamma_2|/\kappa$.

TOPOLOGICAL DEFECT IDENTIFICATION AND TRACKING

We here present our algorithm for locating topological defects, identifying their sign, and tracking their motion. To locate the defects at a given time t, we compute the zero-contours of $\lambda(t, \boldsymbol{r})$ and $\mu(t, \boldsymbol{r})$ in Matlab. Since defects are located at points for which $\lambda = \mu = 0$, we then find the points (x_i, y_i) at which the zero-contours intersect. For each defect, its charge q is determined by computing the rotation of the director angle θ around a closed counterclockwise contour C enclosing the defect. Specifically,

$$q = \frac{1}{2\pi} \oint_C \mathrm{d}\theta, \quad \text{where} \quad \theta = \text{angle}(\boldsymbol{n}) = \tan^{-1}\left(\frac{\mu}{\lambda + \sqrt{\lambda^2 + \mu^2}}\right). \tag{22}$$

We use a square contour and determine its size s as follows. We first construct a $m \times m$ matrix R with entries

$$R_{ij} = \max\left[d_L(x_i, x_j), d_L(y_i, y_j)\right], \tag{23}$$

where $d_L(x, y) = \min(|x - y|, L - |x - y|)$ for $x, y \in \mathbb{R}$ is the periodic Euclidean metric in 1D and L is the size of the simulation box. We then define the size s_i of the contour around the ith defect as

$$s_i = \frac{1}{2}\left(\min_{j<i} R_{ij}\right). \tag{24}$$

We then compute the nematic director angle θ at each grid point on C and thus determine its rotation around C. A rotation by π radians corresponds to a $+1/2$–defect, by $-\pi$ radians to a $-1/2$–defect. We observe that this method works quite well, but occasionally fails to accurately locate and identify defects near the locations of creation and annihilation. During such instances, the net charge is nonzero, and the algorithm detects some spurious defects (indexed by $i = i_1, \ldots i_r$) for which s_i is less than the simulation grid size. Since we initialize the simulations in configurations with zero total charge, we remedy this by placing a single defect of the appropriate sign at the location (x_k, y_k) where

$$k = \arg \min_{l=i_1,\ldots,i_r} \sum_{n=1}^{r} R_{l i_n}. \tag{25}$$

Once the defect locations at every time step are identified, we track their trajectories using the James Munkres' variant of the Hungarian assignment algorithm in Matlab [3]. Specifically, let (x_i^+, y_i^+) be the $+1/2$–defect locations at a time step and $(\tilde{x}_j^+, \tilde{y}_j^+)$ those at the next time step, where $1 \le i \le I$ and $1 \le j \le J$. Let A be the $I \times J$ matrix with entries

$$A_{ij} = \sqrt{d_L(x_i, \tilde{x}_j)^2 + d_L(y_i, \tilde{y}_j)^2}, \tag{26}$$

which corresponds to the periodic Euclidean distance between pairs of defects. An assignment of K pairs is a set of indices $\{(i_k, j_k)\}_{k=1}^{K}$ in the intervals $1 \le i_k \le I$ and $1 \le j_k \le J$ that minimizes the cost measure

$$W = \sum_{k=1}^{K} A_{i_k j_k} + \Upsilon \tag{27}$$

subject to the constraints $i_a \ne i_b$ and $j_a \ne j_b$ for $a \ne b$, where Υ is the cost of unassigned defects. That is, the defects (x_{i_k}, y_{i_k}) are assigned to $(\tilde{x}_{j_k}, \tilde{y}_{j_k})$ for $1 \le k \le K$, and the rest are unassigned. To ensure that $K = \min(I, J)$, or that all available defects are assigned to each other, we take

$$\Upsilon = \max_{i,j} A_{ij} + 1. \tag{28}$$

The same is done for the $-1/2$–defects, and the defect tracks are thus constructed iteratively. New tracks are created from the unassigned defects when $J > I$ or ended when $J < I$. Note that this method assumes that defect pair creation and annihilation events do not occur simultaneously, for which one track should be created and one ended despite $I = J$. Figure S2 shows an example of the computed defect paths for a particular set of simulation parameters.

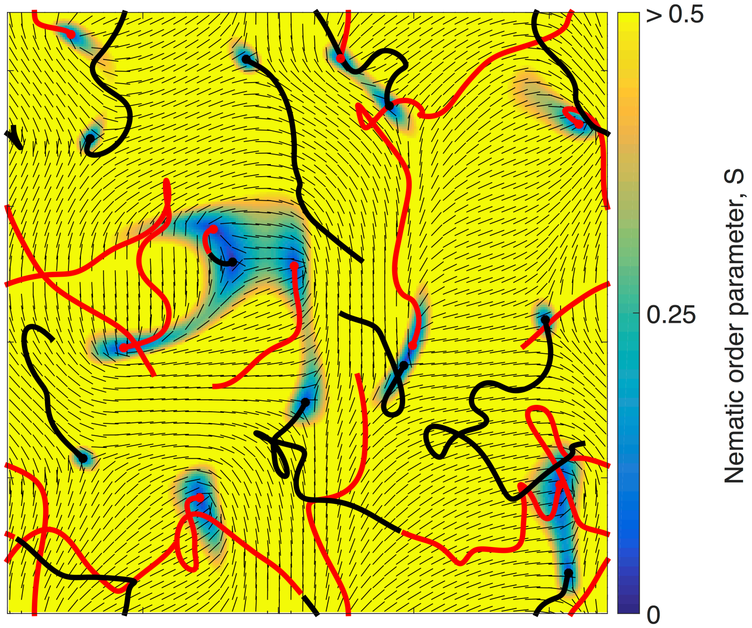

Fig. S2: Example of the computed defect paths using the algorithm described in the text. The color bar shows the nematic order parameter S. The red curves show the trajectories of the $+1/2$–defects, and the black curves the $-1/2$–defects. The simulation parameters correspond to those used in Fig. S3.

MODELING ALIGNMENT NEAR BOUNDARIES

It was found that high-density solutions of actin filaments in rectangular chambers are sensitive to changes in the size and aspect ratio of the confining chamber, as the filaments typically align parallel to the long walls [4]. We here include an effective short-range alignment potential in our model for ALCs, with a view to determining whether the observed orientational order of $+1/2$–defects is affected by an alignment interaction with the boundaries.

In a square simulation box of size L, we impose an alignment potential on the edges $y = 0$ and $y = L$, so that the nematic vector field is preferentially oriented nearby in the horizontal direction $\hat{\boldsymbol{x}} = (1, 0)$. To do this, we append the terms $-f(y)\partial G/\partial\lambda$ and $-f(y)\partial G/\partial\mu$ to the right hand sides of the governing equations (12) for $\lambda(t, \boldsymbol{r})$ and $\mu(t, \boldsymbol{r})$, respectively, where

$$f(y) = \sum_{n=-M}^{M} \mathrm{e}^{-(y-Ln)^2/\sigma^2} \quad \text{and} \quad G(\lambda, \mu) = c(\boldsymbol{n}\cdot\hat{\boldsymbol{x}})^2((\boldsymbol{n}\cdot\hat{\boldsymbol{x}})^2 - 2), \quad c > 0, \quad 0 < \sigma \ll 1. \tag{29}$$

The expression for the nematic vector field $\boldsymbol{n}$ is given in (13). Note that $f(y) \approx 1$ in small horizontal strips around $y = 0$ and $y = L$ and is nearly zero otherwise. The function $G(\lambda, \mu)$ may be interpreted as a potential with minima at $\boldsymbol{n}\cdot\hat{\boldsymbol{x}} = \pm 1$, which causes the vector field to align horizontally. While this approach is rather *ad hoc*, it provides a simple theoretical model for alignment interactions near solid boundaries. A more thorough investigation of boundary interactions should be conducted in the future, perhaps through incorporating a boundary condition directly on the nematic order tensor $Q(t, \boldsymbol{r})$.

Figure S5**a** shows the local pair orientation probability distribution of $+1/2$–defect orientations in a simulation with the alignment potential. Figures S5**b**,**c** compare the corresponding polar $P(r)$ and nematic $N(r)$ correlation functions with those in a simulation without an alignment potential, as shown in Figure 6**c**,**d** in the Main Text. We note that both sets of simulations exhibit antipolar ordering of $+1/2$–defect orientations, and that the degree of orientational order is not significantly altered by including the alignment potential.

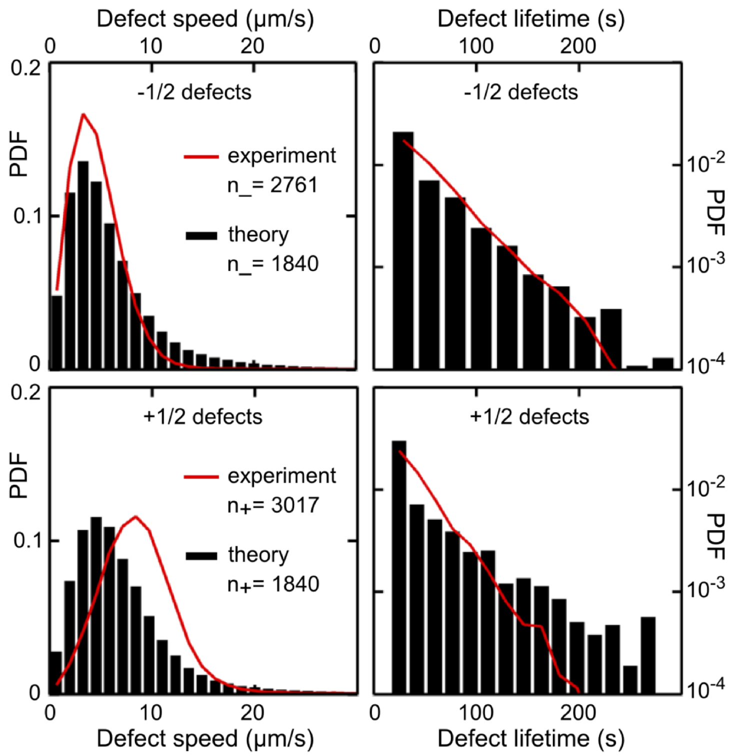

Fig. S3: Quantitative comparison of defect statistics between theoretical predictions (with $\kappa = 0$) and experiment [1], using the parameter estimation procedure described in the Main Text. The simulation domain is nine times smaller in area compared to that in Figure 7 in the Main Text, the other parameters being equal. Top row: For $-\frac{1}{2}$-defects, both speed distribution and lifetime distribution agree well. Bottom row: For $+\frac{1}{2}$-defects, experimentally measured speed values are slightly larger, as our model assumes a strongly overdamped limit. The numbers $n_{\pm}$ reflect the total number of $\pm\frac{1}{2}$-defects tracked. Note that the defect lifetime and speed statistics closely resemble those in Figure 7 of the Main Text, indicating that they are not very sensitive to the size of the periodic simulation domain.

SPATIAL RESOLUTION OF NUMERICAL SIMULATIONS

The numerical simulations were performed with $N = 256$ points in each spatial direction. Fig. S6 shows the power spectra of the functions $\lambda(t_{\mathrm{f}}, \boldsymbol{r})$ and $\mu(t_{\mathrm{f}}, \boldsymbol{r})$ at the final time t_{f} of a sample simulation run. Note that the power decays to a level close to machine precision at high wavenumbers, indicating that $N = 256$ is sufficient to resolve the numerical solution in space.

[1] S. J. DeCamp, G. S. Redner, A. Baskaran, M. F. Hagan, and Z. Dogic, Nature Materials **14**, 1110 (2015).
[2] A. Baskaran and M. C. Marchetti, Phys. Rev. E **77**, 011920 (2008).
[3] J. Munkres, J. Soc. Indust. Appl. Math. **5**, 32 (1957).
[4] J. Alvarado, B. M. Mulder, and G. H. Koenderink, Soft Matter **10**, 2354 (2014).

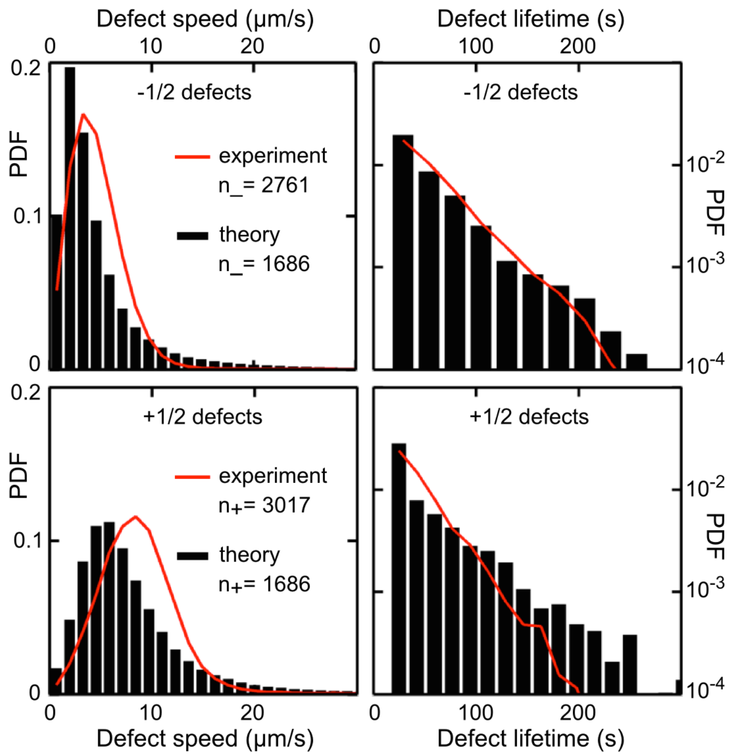

Fig. S4: Quantitative comparison of defect statistics between theoretical predictions (with $\kappa = 1$) and experiment [1], using the parameter estimation procedure described in the Main Text. Top row: For $-\frac{1}{2}$-defects, both speed distribution and lifetime distribution agree well. Bottom row: For $+\frac{1}{2}$-defects, experimentally measured speed values are slightly larger, as our model assumes a strongly overdamped limit. Dimensionless simulation parameters $D = 1.75$ and $\gamma_2 = 1$ translate into the following dimensional values: $a = 0.02\,\mathrm{s}^{-1}$, $b = 0.09\,\mathrm{s}^{-1}$, $D = 869\,\mu\mathrm{m}^2/\mathrm{s}$, $\gamma_2 = 497\,\mu\mathrm{m}^2/\mathrm{s}$, $\gamma_4 = 2.7 \times 10^6 \mu\mathrm{m}^4/\mathrm{s}$. The numbers $n_\pm$ reflect the total number of $\pm\frac{1}{2}$-defects tracked.

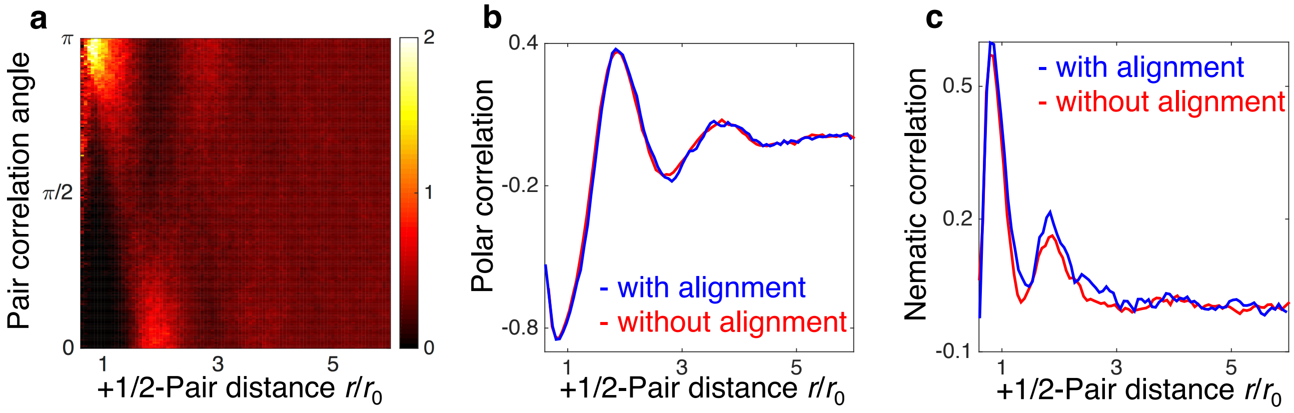

Fig. S5: Orientational order of +1/2–defect orientations in a simulation with an alignment potential imposed at the horizontal edges of the simulation box, as described in the Supplementary Information. The dimensionless simulation parameters are $D = 1.5$ and $\gamma_2 = 2$, and the parameters for the functions defined in eq. (29) are $c = 5$, $M = 2$ and $\sigma = 0.1$. (**a**) Local pair orientation PDF $p(\theta_{ij}|r)$ signals antipolar ordering of+1/2–defects, and reflects the typical defect-lattice spacing in units of the mean nearest-neighbor distance r_0 between $+\frac{1}{2}$–defects. (**b**) The polar correlation function $P(r)$, both with the alignment potential (blue) and without (red, Fig. 6**c** of Main Text). (**c**) The nematic correlation function $N(r)$, both with the alignment potential (blue) and without (red, Fig. 6**d** of Main Text). The plots show that that the degree of orientational order is not significantly altered by the alignment potential.

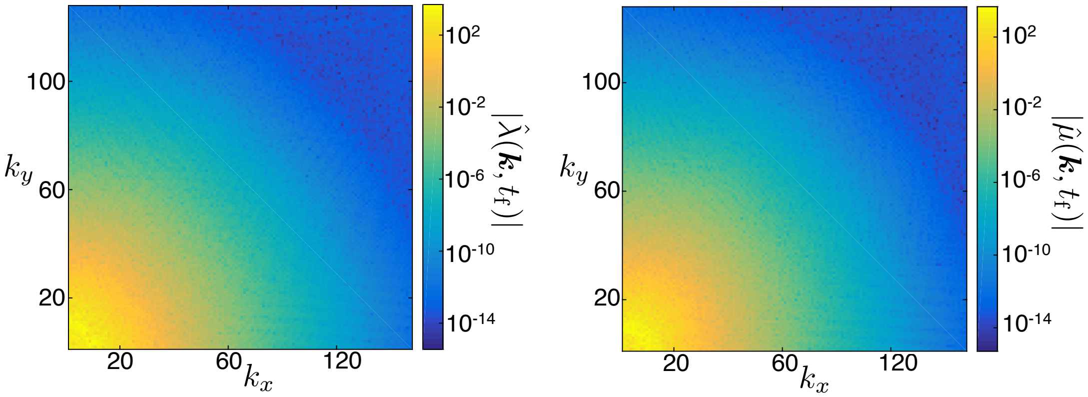

Fig. S6: Power spectra of $\lambda(t_\mathrm{f}, \boldsymbol{r})$ and $\mu(t_\mathrm{f}, \boldsymbol{r})$ for a simulation with dimensionless parameters $D = 1.5$, $\kappa = 0$ and $\gamma_2 = 2$, where t_f is the maximum simulation time. The simulation is performed with $N = 256$ points in each spatial direction. The high frequency modes have power close to machine precision, indicating that the numerical solution is sufficiently resolved in space.